Chemical Engineering Journal 466 (2023) 143139

Contents lists available at ScienceDirect

Chemical Engineering Journal

journal homepage: www.elsevier.com/locate/cej

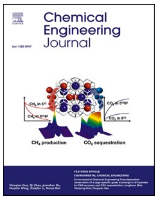

Structural flexibility in cationic metal–organic framework for boosting ReO$_4^-$ capture

Shufen Gu[a], Zhiwu Yu[b], Ning Li[b], Qingyun Zhang[a], Huiping Zhang[a], Lipeng Zhang[c], Lele Gong[c], Rajamani Krishna[d], Feng Luo[a,*]

[a] *School of Chemistry, Biology and Material Science, East China University of Technology, Nanchang 330013, China*
[b] *High Magnetic Field Laboratory, Chinese Academy of Sciences, Hefei 230031, Anhui, China*
[c] *State Key Laboratory of Organic–Inorganic Composites, Beijing Advanced Innovation Center for Soft Matter Science and Engineering, College of Chemical Engineering, Beijing University of Chemical Technology, Beijing 100029, China*
[d] *Van't Hoff Institute for Molecular Sciences, University of Amsterdam, Science Park 904, 1098 XH Amsterdam, the Netherlands*

ARTICLE INFO

Keywords:
Flexible materials
Deformation
cationic MOF
ReO$_4^-$ capture

ABSTRACT

ReO$_4^-$, as a typical anion, its capture is now receiving increasing attentions. However, there still lacks effective method to boost the uptake performance of materials, except for designing new materials. In this work, we found that the structural flexibility could be a good candidate to boost ReO$_4^-$ uptake. The used flexible cationic MOF, $[Co(H_2O)_2(TIB)][NO_3]_2$ (named as **Co-TIB-NO$_3$**, TIB = 3,3′,5,5′-tetra(1H-imidazol-1-yl)-1,1′-biphenyl), showed a multiple response towards temperature, counterion, and solvents with the observation of three different structures, including crystalline OP (open pore) phase, crystalline CP (closed pore) phase, and amorphous CP phase. The origin of the structural flexibility is quite complicated, involving a cage-to-channel migration for counterion, interlayer compression, and deformation of organic ligands. The developed material, **Co-TIB-NO$_3$-313**, showing the amorphous CP phase, was found to perform outstanding ReO$_4^-$ capture with a high uptake capacity, rapid adsorption rate, large distribution coefficient, excellent selectivity, and recyclability, suggesting its superior application in ReO$_4^-$ capture.

1. Introduction

Metal-organic frameworks (MOFs), built on metal nodes and organic ligands through coordination bonds, still remain the frontiers of science and technology, and have been receiving interests, due to their potential applications in many fields such as storage, separation, radioactive treatment, and so on [1–16]. Solvent removal following synthesis, usually results in a rigid MOF structure, with retention of permanent porosity. By contrast, a small number of MOFs about 100 cases from 70,000 MOFs were found to show a dynamic structure, when subjected to external stimuli such as heat, light, pressure, or guest adsorption/desorption [17–31]. This small family are termed as flexible MOFs or soft porous crystals in the literature; their structural flexibility often brings improved performance or exceptional applications that could not be accessed for rigid MOFs [17–31].

Typically, the structural flexibility in MOFs can be classified as 'breathing', 'swelling', subnetwork displacement, rotation of organic ligands, deformation of organic ligands (Scheme 1), and so on [20,32]. Among these, 'breathing' MOFs were commonly encountered, generally featuring a reversible structural transition between open-pore (**OP**) and closed-pore (**CP**) form. The representative example is MIL-53 [33,34]. In a few instances we encounter 'swelling' MOFs or continuous breathing mode, and the antetype is MIL-88 [35]. Subnetwork displacement only occurs in interpenetrating or 2D layer nets [20,32]. Ligand-based approach such as rotation or deformation is strongly dependent on the flexibility of organic ligands [36–39]. Moreover, frustrated flexibility was reported recently, stemming from an incompatibility of intra-framework dispersion forces with the geometrical constraints of the inorganic building units [40]. And Bennett *et al* reported an interesting flexibility phenomenon, transfering crystalline MOFs to be amorphous MOFs or glass-MOFs [41,42].

In fact, ionic MOFs also account for a certain proportion among all established MOFs [43]. A lot of cationic MOFs have been shown as promising anion-exchange materials [44]. Generally speaking, besides electrostatic interaction, counterions in ionic MOFs are also found to weakly bind to framework upon non-covalent interactions. And the

---

* Corresponding author.
E-mail address: ecitluofeng@163.com (F. Luo).

https://doi.org/10.1016/j.cej.2023.143139
Received 11 January 2023; Received in revised form 7 April 2023; Accepted 20 April 2023

presence of counterion will certainly affect and largely complicate the host–guest chemistry, since it will cover a more complicated ternary inter-relationship among counterion, guest molecule, and host framework, rather than the relatively simple binary host–guest relationship in the neutral MOF [45]. This aspect, in conjunction with structural flexibility, will generate a more complicated but extremely interesting system (flexible ionic MOFs) [25,46]. However, several challenges still hinder us from gaining deeper insight into this category, such as the structural characterization of dynamic behaviour for both counterion and framework under external stimuli [25,46].

Herein we represent an intriguing flexible MOF, showing a cationic layer-pillared framework with NO_3^- counterions. The structural flexibility, as unveiled by single/powder crystal X-ray diffraction and theoretical calculation, was responsive to temperature, counterion, and solvents, allowing deeper insights into flexible ionic MOFs (Scheme 1). In addition, we further observed that such flexibility can largely enhance anion-exchange ability, capable of effectively capturing ReO_4^- ions.

2. Experimental section

2.1. Materials and general methods

The reagents and solvents were commercially available and were used as received without further purification. Thermogravimetric analysis (TG) was performed by a TGA Q600 thermal analysis system. All TGA experiments were performed under air atmosphere from 25 °C to 800 °C at a rate of 10 °C /min. X-ray powder diffraction were collected by a Bruker AXS D8 Discover powder diffractometer at 40 kV, 40 mA for Cu Kα (λ = 1.5406 Å) at room temperature in the range of 5–30° (2 theta). The gas sorption isotherms were collected on a Belsorp-max. Ultrahigh-purity-grade (>99.999%) N_2 gas was used in this adsorption measurement. To maintain the experimental temperatures, liquid nitrogen (77 K) was used. SEM was performed by FEI NanoSEM450. X-ray photoelectron spectroscopy (XPS) analysis was carried out through a ESCALAB 250Xi spectrometer with AlKα radiation. ReO_4^- concentration in solutions was measured by both UV/visible spectra and inductively coupled plasmaoptical emission spectroscopy (ICP-OES). ICP-OES tests were carried out by Thermo 7400. The solid state ^{13}C NMR spectra was recorded on a Bruker Avance III WB-400 instrument with a Larmor frequency of 100.65 MHz.The Fourier transform infrared spectroscopy (FTIR) spectra in the range of 4,000–600 cm^{-1} region were acquired on a Thermo Nicolet iS50 spectrometer. Single-crystal diffraction data was collected with variable temperature double target X-ray Single Crystal Diffractometer (Bruker). β-Irradiation was provided by an electron accelerator located at the CGD Dasheng Electron Accelerator Co. Ltd. in Jiangsu Province, China.

2.2. Synthesis of Co-TIB-NO_3

A mixture of 3, 3′, 5, 5′-tetra(1H-imidazol-1-yl)-1, 1′-biphenyl (TIB) (0.024 mmol, 10 mg) and $Co(NO_3)_2{\cdot}6H_2O$ (0.052 mmol, 15 mg) in the 4 mL mixture of DMF and MeCN (v/v:3:1) was sealed in a Teflon lined Parr autoclave. The solution was heated at 130 °C for 3 days followed by decreasing to room temperature within 2 days. After filtration and washed with excess of DMF, orange crystals of **Co-TIB-NO_3** were collected as a pure phase with yield of 80% based on Co. Element analysis: calc. C/46.13%, N/21.35%, H/4.85%, exp. C/46.16%, N/21.40%, H/4.79%. Based on TG and element analysis, the solvent molcules are estimated to be 2.5 DMF molecules in **Co-TIB-NO_3**.

2.3. Synthesis of Co-TIB-Cl

It was prepared by directly soaking 20 mg **Co-TIB-NO_3** crystals in 15 mL 3 M of NaCl solution at room temperature for 24 h. Element analysis: calc. C/33.73%, N/13.11%, H/6.13%, exp. C/33.82%, N/13.18%, H/6.20%. Based on TG and element analysis, the solvent molcules are estimated to be 15 water molecules in **Co-TIB-Cl**.

2.4. Synthesis of Co-TIB-NO_3-313 and Co-TIB-Cl-313

Crystals of **Co-TIB-NO_3** or **Co-TIB-Cl** was degassed under vacuum at 313 K for 24 h, generating **Co-TIB-NO_3-313** and **Co-TIB-Cl-313**, respectively.

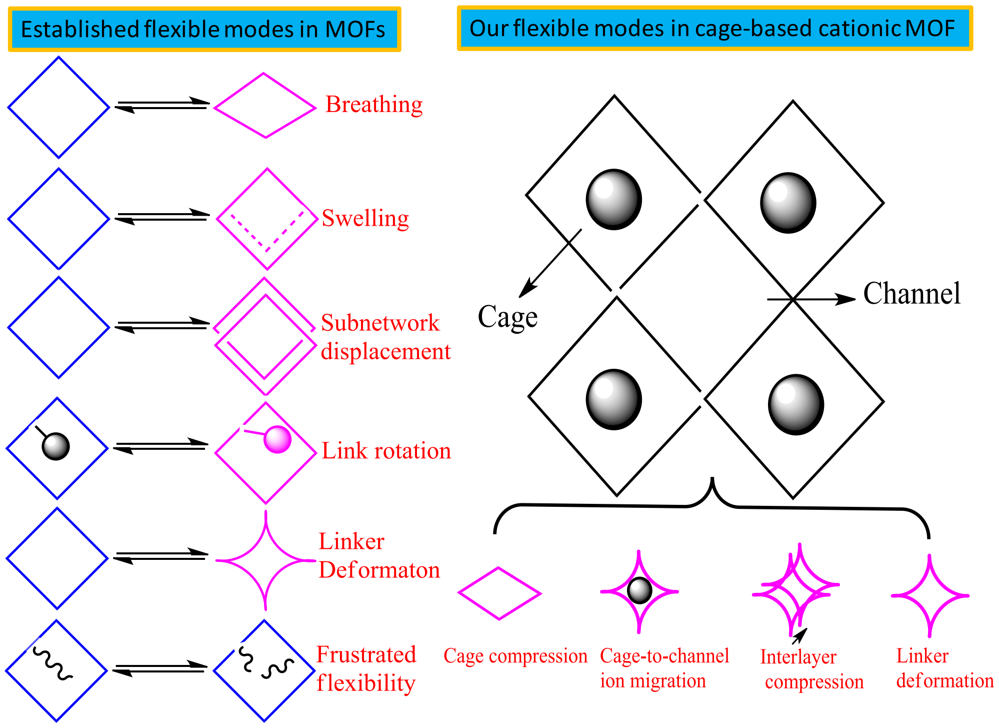

Scheme 1. A draft of flexible modes in MOFs with a comparison of established one in the literature and our case.

3. Results and discussion

3.1. Synthesis, structure and characterizations of Co-TIB-NO_3

The rectangular platelet single crystal of **Co-TIB-NO_3** was synthesized by solvothermal reaction of $Co(NO_3)_2$ and TIB in DMF/CH_3CN at 130 °C. The yield is about 80% based on Co. The phase purity of as-synthesized samples was confirmed by powder X-ray diffraction (PXRD) and subsequent refinement (Fig. S1). The structure of **Co-TIB-NO_3** was determined by single crystal X-ray diffraction at 298 K, showing tetragonal crystal system with *I4/mcm* space group and unit cell parameters of $a = b = 18.2441(10)$ Å, $c = 26.915(4)$ Å, $V = 8958.6(17)$ Å^3. Co ions in this MOF is +2 valence, confirmed by XPS (X-ray photoelectron spectroscopy, Fig. S2), while TIB ligand is neutral, thus creating a cationic framework. The counterions are NO_3^- ions, trapped in a $Co_2(TIB)_4$ cage in an exceptional tetramer arrangement. $Co_2(TIB)_4$ cage made up of two Co(II) ions and four TIB ligands shows a 'wind leaf' configuration (Fig. 1a). The Co-Co distance in this $Co_2(TIB)_4$ cage is 7.93 (2) Å. Each Co(II) ion displays six coordination in an octahedral geometry, finished by four nitrogens from four TIB ligands and two terminal water molecules. The Co-N length is 2.06 (5) Å, while Co-O length for the coordinated water molecule within $Co_2(TIB)_4$ cage is 2.14 (5) Å, shorter than that outside $Co_2(TIB)_4$ cage (2.76 (5) Å). For each TIB ligand, the central biphenyl structure shows perfect co-plane with dihedral angle of 0 (2)°, whereas distortion is observed between the four surrounding imidazole rings and the central biphenyl unit, as evidenced by the torsion angle of 30.0 (2)°, showing the *anti-anti* coordination mode (Fig. 1b).

The secondary building block in this MOF is $Co_2(TIB)_4$ cage, showing a small cavity with size of 3.66 Å×8.89 Å×8.89 Å that was occupied by four NO_3^- counterions in an tetramer arrangement (Fig. 1c), where each NO_3^- plane is vertical to other two adjacent NO_3^- plane, and one of NO_3^- oxygen atom points to another NO_3^- nitrogen atom in turn with a close O…N contact of ca. 3.00 (2) Å. The interaction between $Co_2(TIB)_4$ cage and tetramer counterions is shown in Fig. 1c, where the coordination water molecules within $Co_2(TIB)_4$ cage located up and down the tetramer plane is found to play a key role in fixing this tetramer through hydrogen-bonded interactions (O…O distance/2.77(2) Å-2.98(2) Å). Additionally, multiple C-H…O hydrogen bonds (3.45(2)-3.76(2) Å) between them makes another contribution to fix this tetramer.

$Co_2(TIB)_4$ cages in *ab* plane through sharing TIB ligands construct a cage-based double layer (Fig. 1d and e). If considering each Co(II) ion and TIB ligand as a node, then the framework can be simplified as a binary four-connecting net with $(4^6)(4^2 8^4)$ topology symbol (Fig. S3). Furthermore, two adjacent double layers with AB stacking fashion can be combined together through just one water bridge along *c* direction, resulting in an overall layer-pillared net. Note that, this layer-pillared net is very different from all established examples in the literature [47], and represents the first one solely pillared by water bridges. The distance calculated from the closest metal-to-metal distance between two adjacent layers is about 5.53(2) Å. Moreover, two regular 1D channels are also observed, one being square channel along *c* direction with pore size of 10.3 Å × 10.3 Å, the other one being narrow channel with pore size of 2.7 Å × 12.9 Å along *a* and *b* direction (Fig. S4).

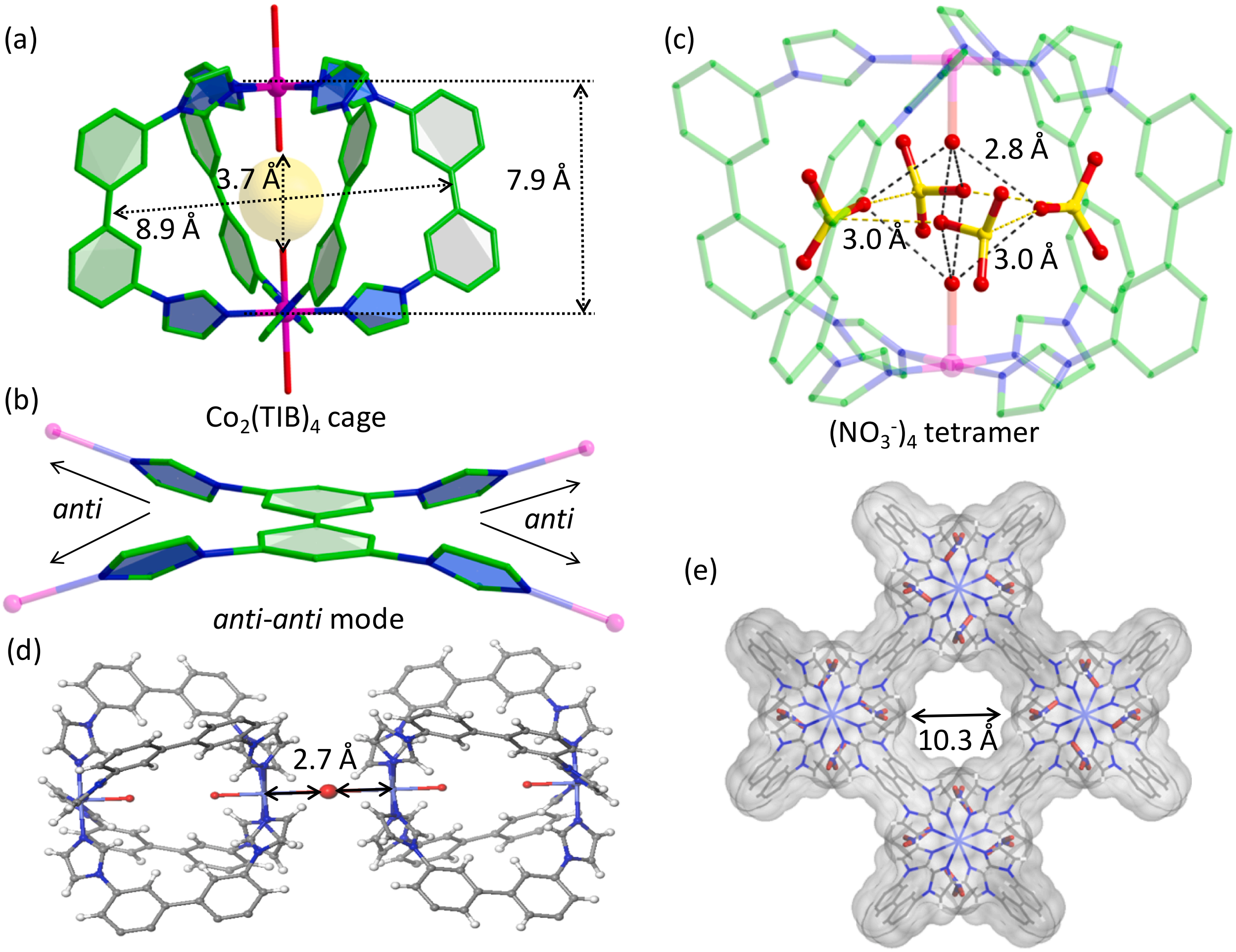

Fig. 1. View of the structures in **Co-TIB-NO_3**. (a) View of $Co_2(TIB)_4$ cage composed of two Co(II) ions and four TIB ligands. (b) The coordination configuration of TIB ligand. (c) The $(NO_3^-)_4$ tetramer in $Co_2(TIB)_4$ cage. (d) The water bridge between two adjacent $Co_2(TIB)_4$ cages. (e) The square 1D channel along *c* direction.

3.2. Anion-exchange of NO_3^- by Cl^-

Soaking **Co-TIB-NO_3** crystals in NaCl solution resulted in a completely Cl-replaced phase of **Co-TIB-Cl**. The structure of **Co-TIB-Cl** determined at 298 K is similar to **Co-TIB-NO_3** (Table S1). However, the location of counterions showed some difference. In **Co-TIB-Cl**, Cl^- counterions were found to locate in not only $Co_2(TIB)_4$ cage (replacing NO_3^- site), but also 1D square channel (Fig. 2a). Similarly, four Cl^- ions within $Co_2(TIB)_4$ cage formed a Cl_4 tetramer with closest Cl…Cl distance of 3.76(2) Å, which is shorter than corresponding N…N distance of 4.33 (2) Å in $(NO_3^-)_4$ tetramer in **Co-TIB-NO_3**. Besides, to confirm the anion-exchange of NO_3^- by Cl^-, we further carried out a series of characterizations. As shown in Fig. 2b, the most intuitive evidence is the observation of large decrease of oxygen element and emergence of abundant chlorine element in SEM (scanning electron microscope) *plus* element mapping (SEM-EDS) in **Co-TIB-Cl** (Fig. 2b), relative to **Co-TIB-NO_3**. Other evidence can be deduced from IR (infrared spectrum) test (Fig. 2c), showing absence of typical IR bond of NO_3^- at 1383 cm^{-1} and $(NO_3^-)_4$ tetramer at 1661 cm^{-1}, and XPS (Fig. 2d), displaying Cl signal with the absence of NO_3^- signal.

3.3. Response towards temperature stimulus

The structural flexibility of **Co-TIB-NO_3** and **Co-TIB-Cl** under various temperatures was investigated through in-situ temperature varying single crystal X-ray diffraction. For **Co-TIB-NO_3**, it is found that the crystal at 308 K was maintained and showed comparable structure and unit cell parameters of $a = b = 18.1936(6)$ Å, $c = 26.897(2)$ Å, $V = 8903.3(8)$ Å^3, as observed in **Co-TIB-NO_3** (Table S1). But two major differences were observed for TIB ligand and $(NO_3^-)_4$ tetramer (Fig. 3). For TIB ligand, almost bending deformation was observed between two central biphenyl units, as evidenced by the dihedral angle of 52.4 (2)°, while, by contrast, the crystal at 298 K gave corresponding value of 0 (2)°, indicative of structural flexibility from deformation of TIB ligand in response to temperature. At the same time, in contrast to the crystal at 298 K, the distortion of imidazole ring at 308 K, relative to conjoint phenyl ring, is reduced to be 11.0°, implying structural flexibility from rotation of imidazole unit of TIB ligand in response to temperature. As a result, a distinct *syn-syn* coordination configuration was observed for TIB ligand at 308 K. For $(NO_3^-)_4$ tetramer, the determined structure at 308 K becomes ordered, rather than disordered structure at 298 K, and accompanied is the elongated O…N contact of 3.35 (2) Å.

On further increase of temperature to 313 K, the crystals of **Co-TIB-NO_3** will lose crystallinity, as evidenced by PXRD test, displaying broad diffuse scattering (Fig. S5), indicative of non-crystalline state (named as **Co-TIB-NO_3-313**). To disclose the structure of **Co-TIB-NO_3-313**, a series of characterizations were employed, including infrared spectrum (IR), XPS, and solid-state ^{13}C MAS NMR spectra. The $(NO_3^-)_4$ tetramer showing IR bond at 1661 cm^{-1} was observed in **Co-TIB-NO_3**, however this disappeared in **Co-TIB-NO_3-313**, suggesting structural flexibility from disassembly of tetramer counterion in response to higher temperature (Fig. S6); this is most likely due to the migration of NO_3^- from cage to channel. In XPS, the electron binding energy of Co(II) increased to be 781.6 eV in **Co-TIB-NO_3-313**, relative to the value of 780.8 eV in **Co-TIB-NO_3**, implying enhanced coordination bond for Co(II) ions, due to structural flexibility from interlayer compression that reinforces Co-O coordination bond from the water molecule outside $Co_2(TIB)_4$ cage (Fig. S7). An inspection on N element disclosed no obvious change in the electron binding energy of nitrogen for TIB ligand, suggesting the retention of framework (Fig. S8). However, the binding energy of nitrogen from NO_3^- is reduced from 406.3 eV in **Co-TIB-NO_3** to 405.9 eV in **Co-TIB-NO_3-313**, confirming the structural flexibility from disassembly of tetramer counterion (Fig. S8). ^{13}C MAS NMR spectra renders a heterogeneous local structure of non-crystalline phase, as illustrated by the broadened signals of the TIB carbon atoms (Fig. S9). Moreover, we tested N_2 adsorption at 77 K, giving a type IV isotherm with low BET surface area of 60.3 m^2/g and small pore volume of 0.06 cm^3/g (Fig. S10), which is far below the corresponding calculated value of 1628.5 m^2/g and 0.56 cm^3/g from crystal data of **Co-TIB-NO_3**. This is mainly because of the formation of CP form in **Co-TIB-NO_3-313**. The

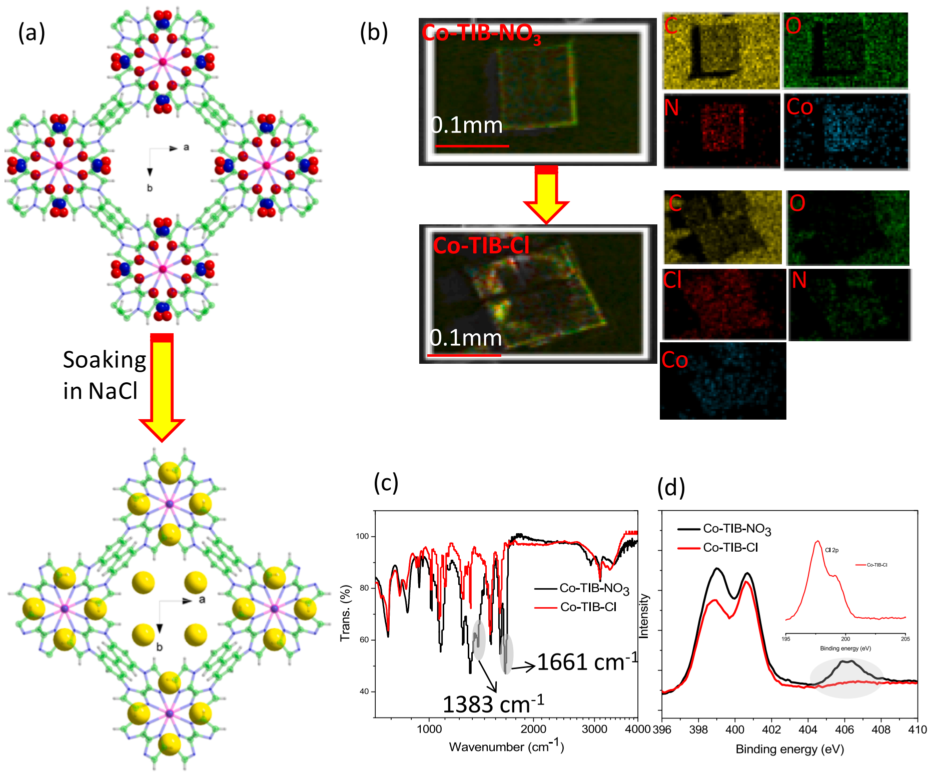

Fig. 2. (a) View of the anion-exchange structure from **Co-TIB-NO_3** to **Co-TIB-Cl**. The yellow spheres are Cl^- ions. (b) A comparison of SEM-EDS between **Co-TIB-NO_3** and **Co-TIB-Cl**. (c) A comparison of IR between **Co-TIB-NO_3** and **Co-TIB-Cl**. The highlight is the typical IR bond for NO_3^- (1383 cm^{-1}) and $(NO_3^-)_4$ tetramer (1661 cm^{-1}). (d) A comparison of XPS between **Co-TIB-NO_3** and **Co-TIB-Cl**. The highlight indicates the complete anion exchange of NO_3^- by Cl^-. Insert is Cl element XPS in **Co-TIB-Cl**. (For interpretation of the references to colour in this figure legend, the reader is referred to the web version of this article.)

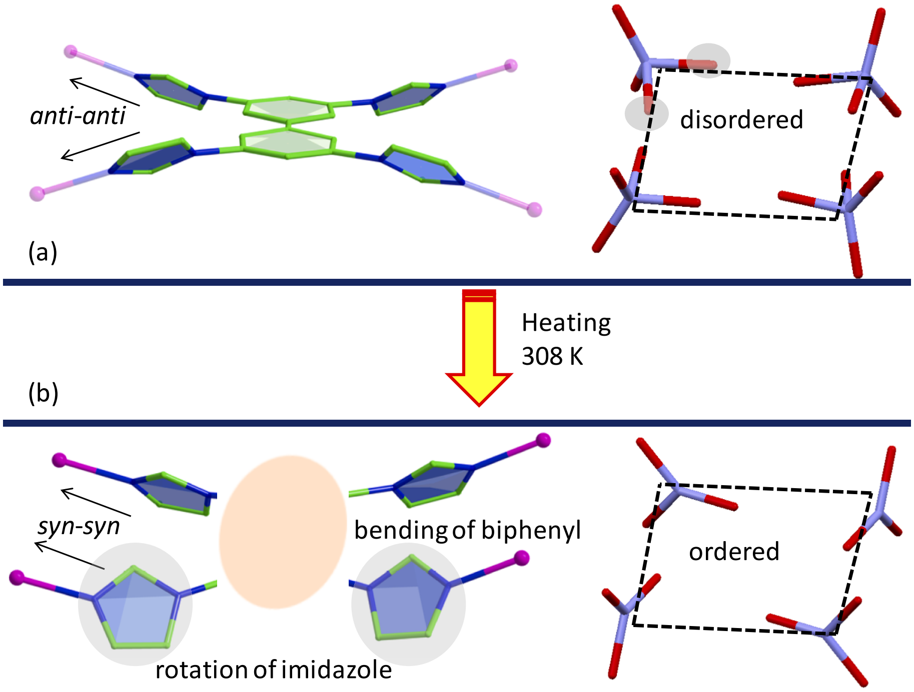

Fig. 3. View of the two major differences in TIB ligand and $(NO_3^-)_4$ tetramer for the crystal determined at 298 K (above) and 308 K (below).

observation of type IV N_2 adsorption stems from the crackle of crystal samples after heating 313 K (see the scanning electron microscope (SEM) results, Fig. S11). Two distinct pores were observed in **Co-TIB-NO$_3$-313** (Fig. S10), one showing narrow pore size distribution with micropore size of 0.37 nm, derived from CP form, the other one being broad pore size distribution with mesopore size of 3.9 nm, due to crackle of crystal samples. Moreover, heating the samples of **Co-TIB-NO$_3$** at 323 K and 333 K also displayed broad diffuse scattering of PXRD (Fig. S12), suggesting non-crystalline state.

On the other hand, for **Co-TIB-Cl**, similar temperature-various single crystal X-ray diffraction was carried out. It is found that heating crystals of **Co-TIB-Cl** at 308 K gave no clear change in the structure. However,

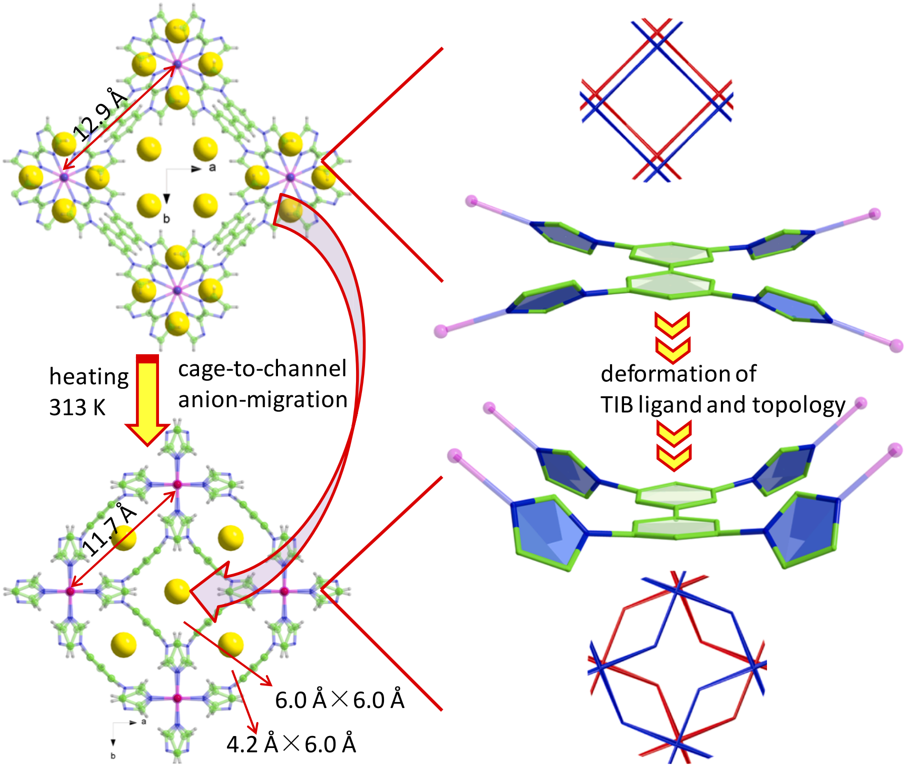

Fig. 4. View of structural flexibility of **Co-TIB-Cl** after heating at 313 K. A comparison of structure between **Co-TIB-Cl** and **Co-TIB-Cl-313** including the location of Cl^- ions, channel, TIB ligand, and the topology matrix.

heating crystals at 313 K would generate a new crystalline phase of **Co-TIB-Cl-313** (Table S1). More interestingly, although the symmetry (tetragonal) and space group (*I4/mcm*) is not changed, however, the unit cell parameters show big difference like that of $a = b = 16.497(2)$ Å, $c = 26.594(6)$ Å, $V = 7238(2)$ Å^3, creating an overall 17% contraction on *ab* plane rather than *c* direction, in contrast to **Co-TIB-Cl**. The main structure was maintained such as the coordination surrounding of metal ion, $Co_2(TIB)_4$ cage, and the framework connectivity. But, obvious difference included deformation of TIB ligand and topology matrix was observed in **Co-TIB-Cl-313**, as evidenced by the dihedral angle of 2.7(2) ° for the central biphenyl structure, the torsion angle of 50.0(2)° for imidazole ring with conjoint phenyl ring, and the *syn-syn* coordination mode of TIB ligand (Fig. 4), relative to **Co-TIB-Cl**. Shorter distance of 11.7(2) Å along *ab* plane between two adjacent $Co_2(TIB)_4$ cage was observed, relative to that of 12.9 Å in **Co-TIB-Cl** (Fig. 4). More impressively, each initial square 1D channel in **Co-TIB-Cl** is divided into four identical rectangle 1D channels with pore size of 4.2 Å × 6.0 Å and one square 1D channel with pore size of 6.0 Å × 6.0 Å in **Co-TIB-Cl-313** along *c* direction, suggesting formation of CP form in **Co-TIB-Cl-313**. Notably, Cl^- ions were found to locate in the center of both rectangle and square 1D channel, indicative of structural flexibility from cage-to-channel counterion-migration in response to temperature, relative to **Co-TIB-Cl**. The solvent-accessible volume was also reduced from 49.1% in **Co-TIB-Cl** to 36.8% in **Co-TIB-Cl-313** [48]. The phase purity of **Co-TIB-Cl-313** was confirmed by PXRD test and next refinement (Fig. S13). XPS of Co element in **Co-TIB-Cl-313** showed almost no detectable change, relative to **Co-TIB-Cl** (Fig. S14), suggesting no flexibility in *c* direction, which is in agreement with the results from crystal data. Moreover, the deformation of TIB ligand and cage-to-channel anion-migration can be also reflected on XPS of N and Cl element (Fig. S15 and S16). N_2 adsorption at 77 K gave a type I isotherm with BET of 312 m^2/g and pore volume of 0.25 cm^3/g (Fig. S17); this value is comparable with the calculated value of 289.9 m^2/g and 0.32 cm^3/g from crystal data, suggesting rigid framework of **Co-TIB-Cl-313**. Two micropores with narrow pore size distribution of 0.45 nm and 0.6 nm was observed (Fig. S17), consistent with the pore size evaluated from crystal data. Moreover, further increasing calcination temperature up to 323 K and 333 K will decrease the crystallinity, but the resultant samples was found to possess similar structure as observed in **Co-TIB-Cl-313** (Fig. S18).

3.4. Recovery to OP form

Interestingly, soaking the non-crystalline form of **Co-TIB-NO$_3$-313** in DMF led to recovery to crystalline OP form of **Co-TIB-NO$_3$**, confirmed by single crystal X-ray diffraction (Table S1). This is mainly because the maintenance of coordination, skeleton in the non-crystalline form, as observed in the crystalline form, and the occurrence of a long-period irregular arrangement induced by heating. By contrast, no recovery was observed for soaking the non-crystalline form (generated at 323 K and 333 K) in DMF (Fig. S19), suggesting certain decomposition of framework under this condition. On the other hand, recovery to OP form was observed for these Cl-replaced samples (generated at 313 K, 323 K, and 333 K) in the crystalline CP form, when soaking them in DMF (Table S1). All the results suggest reversible structural flexibility from CP form to OP form in response to DMF, except for some exceptions such as the non-crystalline form (generated at 323 K and 333 K).

3.5. Simulation and mechanism of framework flexibility

With the aim to achieve a fully atomistic understanding of the framework flexibility, we further carried out DFT calculation by simultaneously compressing the unit cell of *a*, *b*, and *c* [49,50]. The pristine framework of **Co-TIB** derived from **Co-TIB-NO$_3$** with the removal of NO_3^- counterions was used as the initial model. As shown in Fig. 5, it is clear that the crystalline-to-amorphous transition occurs at a compression of *a*, *b*, and *c* with 35%. The amorphization mainly results from the exquisite distortion of TIB ligand. On examination of these simulated structures under 1%-30% compression, smart deformation of TIB ligand was observed, including in rotation of imidazole ring, bending of central biphenyl ring, and swing of imidazole unit (relative to central biphenyl unit). More impressively, the calculated structure under 10% compression with a = b = 16.3742 (10) Å, c = 24.2073 (10) Å, and V = 6490(2) Å, as well as pore configuration and pore size is close to **Co-TIB-Cl-313** (Fig. S20), confirming the validity of our calculation method. Notably, unit cell of a = b = 16.497(2) Å in **Co-TIB-Cl-313** agrees well with the calculated value under 10% compression, while the corresponding volume change of 19.2% in **Co-TIB-Cl-313** is also comparable with the value 27.5% under 10% compression. Moreover, the distortion between imidazole unit and central biphenyl unit is further comparable such as 50.0(2) ° (exp.) vs. 59.4(2) ° (calc.).

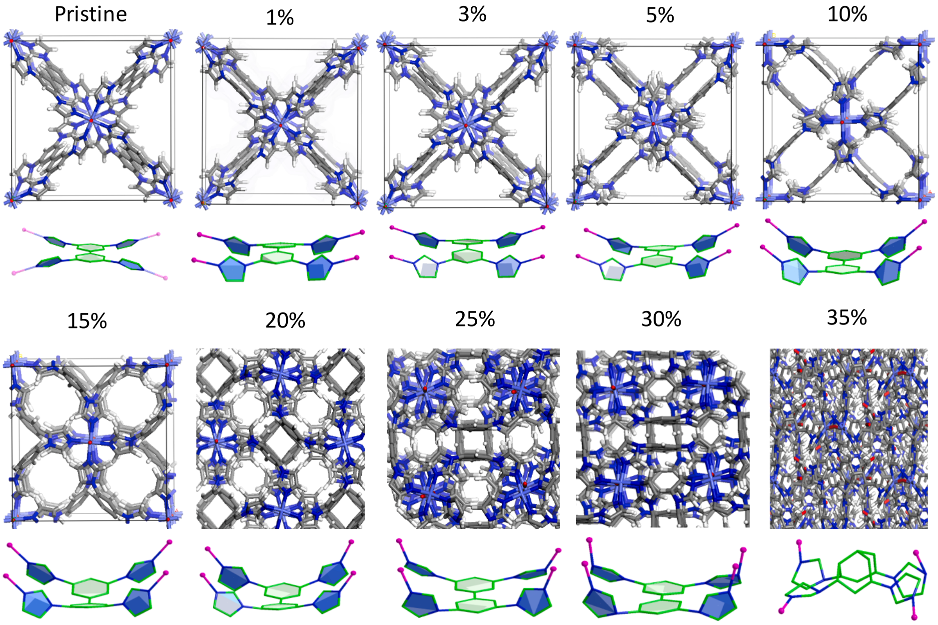

Fig. 5. A comparison of Co-TIB framework and TIB ligand between pristine one and the counterparts under 1%-35% compression in the crystal volume.

3.6. ReO$_4^-$ adsorption

Recent advances disclosed the important application of cationic frameworks in removal of radioactive $^{99}TcO_4^-$contamination [51–62]. It is well known that the removal of $^{99}TcO_4^-$ remains a difficult and challenging task, due to $^{99}TcO_4^-$ with large size, low charge density, high water solubility, high mobility, low binding constant, and small complexing enthalpy. Especially, there is still a lack of a general, simple, and effective method to boost $^{99}TcO_4^-$ removal without the need for design and synthesis of a large number of new cationic frameworks. To this end, the discovery of flexible cationic framework in this work promotes us to investigate its application in $^{99}TcO_4^-$ removal. In light of the radioactive nature of $^{99}TcO_4^-$, herein we employed the commonly used nonradioactive surrogate of ReO$_4^-$ to conduct current research.

We initially investigated the ReO$_4^-$ adsorption by using 10 mg adsorbent and 30 mL NH$_4$ReO$_4$ solution (50 ppm). The results were shown in Fig. 6a. It is found that the sorption equilibrium was achieved within 2 h for all these MOFs. And the sorption data can be well fitted by the pseudo-second-order model (Table S2), giving fast rate constant (k_2, $g \cdot mg^{-1} \cdot min^{-1}$) with hiberarchy of **Co-TIB-Cl** (8.2×10^{-3}) > **Co-TIB-Cl-313** (4.8×10^{-3}) > **Co-TIB-NO$_3$-313** (4.4×10^{-3}) > **Co-TIB-NO$_3$** (3.8×10^{-3}). The results imply that anion exchange of NO$_3^-$ by Cl$^-$ can enhance the sorption rate.

To evaluate the uptake capacity, the adsorption tests over a NH$_4$ReO$_4$ solution from 100 to 600 ppm were carried out. The adsorption isotherm was shown in Fig. 6b (Table S3), where the uptake capacity (mg/g) yields the hierarchy, **Co-TIB-NO$_3$-313** (540.0) > **Co-TIB-Cl-313** (460.7) > **Co-TIB-Cl** (391.7) > **Co-TIB-NO$_3$** (284.2). The results showed that in this system anion-exchange of NO$_3^-$ by Cl$^-$ ions can first boost ReO$_4^-$ removal, then heating at 313 K can further enhance ReO$_4^-$ removal, indicative of the big potential of flexible cationic framework in $^{99}TcO_4^-$ removal. The best adsorption value in **Co-TIB-NO$_3$-313** exceeds most established cationic MOFs (Fig. 6c, Table S4) [63], comparable with the benchmark MOFs such as SCU-100 (541 mg/g) [64] and Th-MOF-68 (560 mg/g) [65]. The distribution coefficient (K_d) of these MOFs toward ReO$_4^-$ reaches 10^4 mL/g with the hierarchy, **Co-TIB-Cl** (9.3×10^4) > **Co-TIB-NO$_3$** (9.1×10^4) > **Co-TIB-NO$_3$-313** (2.0×10^4) > **Co-TIB-Cl-313** (1.7×10^4). The K_d values are noticeably higher than for most reported anion sorbent materials such as Mg-Al-LDH [66] and comparable with some benchmark anion sorbent materials like that of SCU-100 [64]. We further explored the anion-exchange selectivity of these MOFs in the presence of one equivalent of NO$_3^-$, CO$_3^{2-}$, PO$_4^{3-}$, ClO$_4^-$, and SO$_4^{2-}$ with concentration of 125 ppm (Figs. S21-S23). Among them, **Co-TIB-NO$_3$-313** affords excellent ReO$_4^-$ selectivity towards all used anions (Fig. 6d), as evidenced by the little reduction in the ReO$_4^-$ uptake under mixed anions, relative to that just under ReO$_4^-$. By contrast, PO$_4^{3-}$ shows the biggest effect on the ReO$_4^-$ uptake with a 26% decrease in **Co-TIB-NO$_3$**, while correspondingly, 20% and 31% decrease respectively caused by NO$_3^-$ and CO$_3^{2-}$ were observed in **Co-TIB-Cl** and **Co-TIB-Cl-313**. In addition, the desorption of ReO$_4^-$ into solution can be simply achieved by soaking in 3 M NaNO$_3$ for or NaCl solution for nitrate- and chlorine-containing materials, respectively. The desorption efficiency is over 93% for all these MOFs. Good recycle use was observed for all these MOFs (Figs. S24-S27), as evidenced by negligible decrease in the ReO$_4^-$ removal after repeating five adsorption–desorption circle. All the above results imply the significant potential of these MOFs, especially **Co-TIB-NO$_3$-313**, in elimination of radioactive $^{99}TcO_4^-$ contamination.

3.7. Stability of adsorbents

For practical application, the stability of adsorbents under water and irradiation represent an important consideration. In this regard, **Co-TIB-NO$_3$-313** and **Co-TIB-Cl-313** were representatively selected. For **Co-TIB-NO$_3$-313**, phase transition from amorphous CP form to crystalline CP from was observed, when soaking it in water with pH = 1, 7, and 10 (Fig. S28). By contrast, no change was observed for **Co-TIB-Cl-313** under similar conditions, suggesting the retention of crystalline CP form (Fig. S29). Moreover, decomposition was observed for both **Co-TIB-NO$_3$-313** and **Co-TIB-Cl-313**, when pH value is more than 11. In order to obtain the general applicability of adsorbents, we further tested the ReO$_4^-$ uptake for both **Co-TIB-NO$_3$-313** and **Co-TIB-Cl-313** under various pH values (Figs. S30-S31), giving slight effect on ReO$_4^-$ uptake under acidic condition and big effect on ReO$_4^-$ uptake under alkaline condition. Furthermore, the irradiation tolerance of adsorbents was

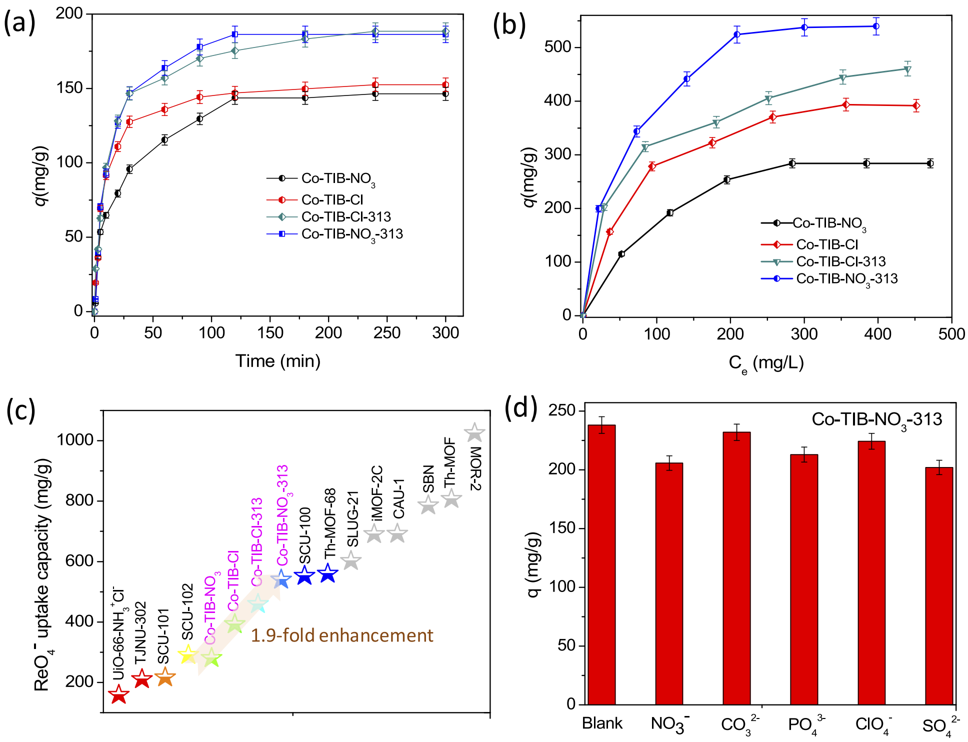

Fig. 6. The ReO$_4^-$ capture research in this work. (a) Sorption kinetics of ReO$_4^-$ by **Co-TIB-NO$_3$**, **Co-TIB-NO$_3$-313**, **Co-TIB-Cl**, and **Co-TIB-Cl-313**. (b) Sorption isotherms of ReO$_4^-$ by **Co-TIB-NO$_3$**, **Co-TIB-NO$_3$-313**, **Co-TIB-Cl**, and **Co-TIB-Cl-313**. (c) A comparison of ReO$_4^-$ uptake capacity between some outstanding cationic MOF sorbents and our cases. The highlight renders a 1.9-fold enhancement of ReO$_4^-$ uptake just caused by flexibility. (d) Effect of competing anions on the ReO$_4^-$ uptake by **Co-TIB-NO$_3$-313**.

explored under β-irradiation at a dose rate of 20 kGy/h for 10 h, PXRD tests showed the maintenance of the integrity of the framework, as observed in **Co-TIB-NO$_3$-313** and **Co-TIB-Cl-313** (Fig. S32). β-Irradiation on the samples was also found to have little effect on the ReO_4^- uptake (Fig. S33).

3.8. Phase-dependent adsorption mechanism

In general, cationic framework materials employs anion-exchange mechanism to capture ReO_4^- [51–70]. Undoubtedly, ReO_4^- capture in our MOFs is also mainly based on anion-exchange mechanism. However, as discussed above, our MOFs generated under various conditions showed big difference in ReO_4^- uptake; thus, we anticipated additional contribution on ReO_4^- uptake, except for anion exchange, and further carried out a series of characterizations.

In light of the best performance in ReO_4^- capture using **Co-TIB-NO$_3$-313**, it is representatively selected to carry out other characteriazations including IR, SEM-EDS, and PXRD (Fig. 7). In the ReO_4^- loaded samples (Fig. 7a), the absence of typcial IR bonds of NO_3^- (1383 cm^{-1}) and $(NO_3^-)_4$ tetramer (1661 cm^{-1}) and new formation of IR bond at 903 cm^{-1} (typical for ReO_4^-) [71–77] strongly supports the full anion-exchange of NO_3^- by ReO_4^-. In SEM images (Fig. 7b), we found the retention of rectangular platelet crystal morphology after ReO_4^- uptake, suggesting high chemical and mechanical stability, while uniform distribution of ReO_4^- was observed in EDS mapping. More interestingly, recovery to crystalline state (Fig. 7c) was observed for the samples after ReO_4^- uptake, which is in agreement with CP phase of **Co-TIB-Cl-313**, indicative of ReO_4^- induced phase transformation from non-crystalline **CP** state to crystalline **CP** state. This in conjunction with the experimental results strongly suggests the significant contribution on ReO_4^- removal from structural flexibility of **CP**-to-**CP** transformation. By contrast, no phase transformation was found for **Co-TIB-Cl-313** after ReO_4^- loading, due to the rigid framework in **Co-TIB-Cl-313** (Fig. 7d). As discussed above, the pore volume in **Co-TIB-NO$_3$-313** (0.06 cm^3/g) is far below that in **Co-TIB-Cl-313** (0.25 cm^3/g), thus indicative of a more closed pore in **Co-TIB-NO$_3$-313**, relative to **Co-TIB-Cl-313**; and this to some extent suggests bigger structural flexibility and consequently leads to ultrahigh ReO_4^- uptake in **Co-TIB-NO$_3$-313**. Moreover, we further measured PXRD patterns of ReO_4^- loaded samples for **Co-TIB-NO$_3$** and **Co-TIB-Cl**. Interestingly, no phase transformation was found, in contrast to the pristine samples (Figs. S34-S35). In addition, we further explored ReO_4^- uptake for samples generated at 323 K and 333 K, and a comparison of ReO_4^- uptake for samples generated at various temperature was shown in Figs. S36-S37, giving that further enhancement in ReO_4^- uptake was not observed for these samples after generated at 323 K and 333 K, due to decomposition in NO_3^--containing derivates or similar structural flexibility for Cl$^-$-containing derivates (samples generated at 313 K, 323 K, and 333 K affords the same structure).

In light of the above results, a summary and the and interrelationship among the structural flexibility, stimulus, and ReO_4^- uptake was shown in Fig. 8. It is found that temperature provides the key control on the structural flexibility, which can cause the structural transition from OP to CP form. The type of counterions can further amplify the temperature effect, resulting in large difference in crystallinity, porosity, ReO_4^- uptake ability, and recovery ability from solvent. Moreover, three major factors including increasing the heating treatment temperature, tuning the type of counterion, and improving structural flexibility are found to afford positive effect on ReO_4^- uptake. To obtain a deep insight into the relationship between structural flexibility and ReO_4^- uptake, we further carried out theoretical calculation on the exchange energy (ΔG_a) for samples of **Co-TIB-NO$_3$**, **Co-TIB-Cl**, and **Co-TIB-Cl-313 K**, giving a hierarchy, **Co-TIB-NO$_3$** (−1.36 eV) **>** **Co-TIB-Cl** (−2.05 eV) **>** **Co-TIB-Cl-313 K** (−2.33 eV). The results demonstrated that ReO_4^- ions were most easily substituted for Cl$^-$ ion in **Co-TIB-Cl-313 K** than in **Co-TIB-Cl**, because of the lowest exchange energy ($\Delta G_a = -2.33$ eV) in **Co-TIB-Cl-313 K**, confirming the temperature effect; this also implies the best ReO_4^- uptake for **Co-TIB-Cl-313 K**. In addition, **Co-TIB-NO$_3$** affords the biggest exchange energy ($\Delta G_a = -1.36$ eV), indicative of a relatively poor ReO_4^- uptake, while the exchange energy in **Co-TIB-Cl** relatively lower than that in **Co-TIB-NO$_3$** also strongly supports the positive effect on ReO_4^- uptake from the replacement of NO_3^- counterion of by Cl$^-$. Accordingly, the order of ReO_4^- uptake can be deduced as follows: **Co-TIB-Cl-313 K > Co-TIB-Cl > Co-TIB-NO$_3$**, which is entirely consistent with the experimental results of **Co-TIB-Cl-313 K** (459.6 mg/g) **>** **Co-TIB-Cl** (392.9 mg/g) **>** **Co-TIB-NO$_3$** (281 mg/g).

4. Conclusion

In conclusion, we successfully synthesized a water-bridged pillar-layered cationic MOF by self-assembly of Co(II) ions with neutral multiple N-donor ligands. The counterions were found to locate in the center of Co$_2$(TIB)$_4$ cage in a unique fashion of $(NO_3^-)_4$ or Cl$_4$ tetramer. The

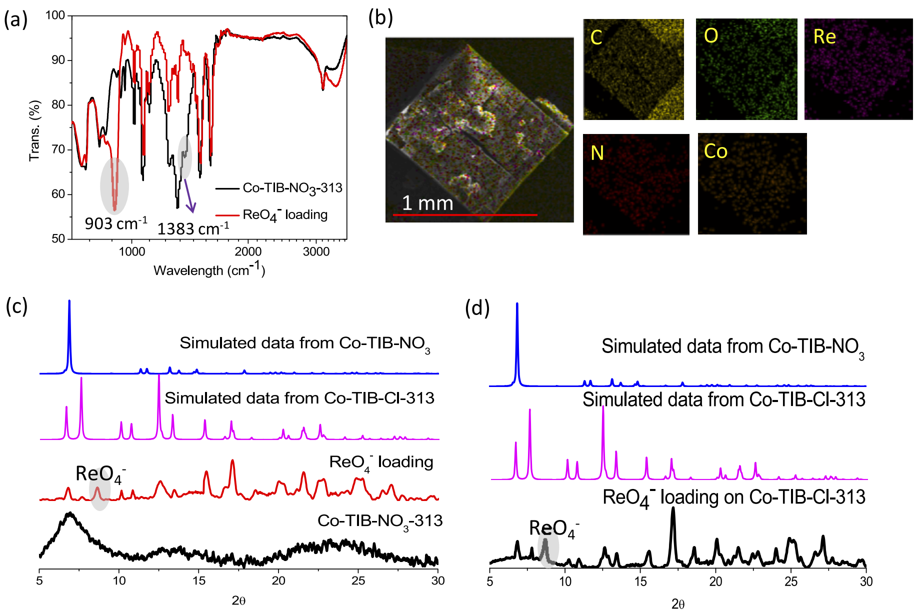

Fig. 7. (a) A comparison of IR between the samples of **Co-TIB-NO$_3$-313** and its ReO_4^- loading counterpart. (b) SEM image and EDS mapping of **Co-TIB-NO$_3$-313** after ReO_4^- loading. (c) A comparison of PXRD patterns among the samples of **Co-TIB-NO$_3$-313**, its ReO_4^- loading counterpart, and the simulated one from the crystal data of **Co-TIB-Cl-313** and **Co-TIB-NO$_3$**. (d) A comparison of PXRD patterns among the samples of **Co-TIB-Cl-313** after ReO_4^- loading and the simulated one from the crystal data of **Co-TIB-Cl-313** and **Co-TIB-NO$_3$**.

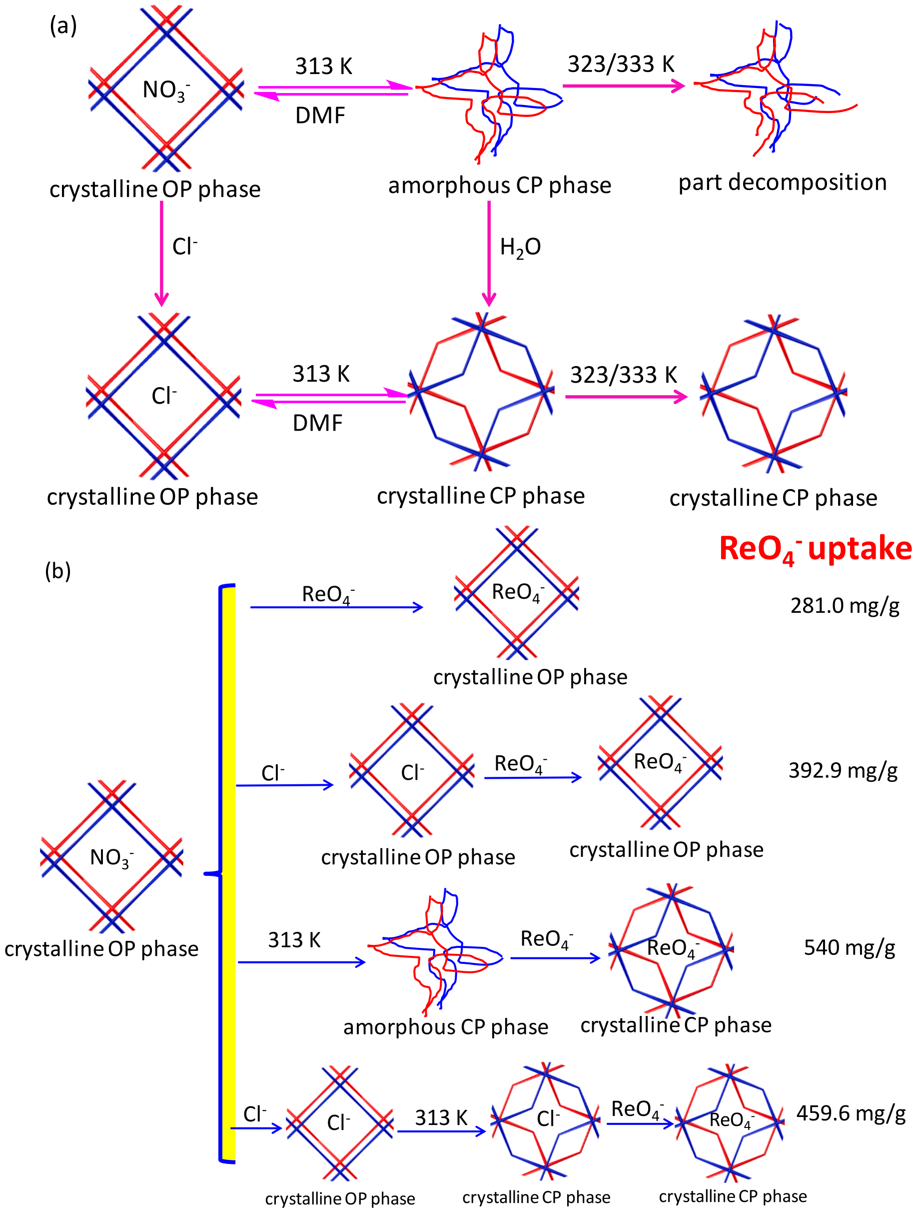

Fig. 8. A summarization and relationship among the structural flexibility, stimulus, and ReO_4^- uptake.

cationic framework renders smart response towards thermal treatment. The temperature 313 K is a key factor that can cause crystalline **OP** to amorphous **CP** phase transition, when NO_3^- ions act as counterion, on the other hand, crystalline **OP** to crystalline **CP** phase transition, when Cl^- ions act as counterion. The origin of the structural flexibility mainly results from (i) weak coordination bond as interlayer bridge that allows for interlayer compression, (ii) mobility of counterions in the solid, and (iii) deformation of organic ligands. The framework flexibility coupled with the cationic nature further gives the materials with distinct response towards guest molecules such as ReO_4^-, for the first time opening up the gate of application of flexible ionic MOFs in eliminating radionuclide pollution. We also believe that the findings in this work will largely promote the design and application of flexible ionic MOFs.

Declaration of Competing Interest

The authors declare that they have no known competing financial interests or personal relationships that could have appeared to influence the work reported in this paper.

Data availability

Data will be made available on request.

Acknowledgment

We thanks to the Training Program for Academic and Technical Leaders of Major Disciplines in Jiangxi Province (20194BCJ22010), the National Natural Science Foundations of China (21966002, 21871047), the Youth leading talent project of FuZhou (NO. 2020ED64), Jiangxi project (DHSQT22021007), and Graduate Innovation Project of East China University of Technology (YC2021-S625).

Appendix A. Supplementary data

Supplementary data to this article can be found online at https://doi.org/10.1016/j.cej.2023.143139.

References

[1] H. Furukawa, K.E. Cordova, M. O'Keeffe, O.M. Yaghi, The chemistry and applications of metal-organic frameworks, Science 341 (2013) 1230444.

[2] G. Chakraborty, I.H. Park, R. Medishetty, J.J. Vittal, Two-dimensional metal-organic framework materials: synthesis, structures, properties and applications, Chem. Rev. 121 (2021) 3751–3891.

[3] H. Jiang, D. Alezi, M. Eddaoudi, A reticular chemistry guide for the design of periodic solids, Nat. Rev. Mater. 6 (2021) 66–487.

[4] L.B. Li, R.B. Lin, R. Krishna, H. Li, S.C. Xiang, H. Wu, J.P. Li, W. Zhou, B.L. Chen, Ethane/ethylene separation in a metal-organic framework with iron-peroxo sites, Science 362 (2018) 443–446.

[5] M. Yin, Q. Zhang, T. Fan, C. Fan, S. Pu, R. Krishna, F. Luo, Selective krypton uptake through trap confinement, formation of Kr_2 dimer, and light response in a photochromic and radiation-resistant thorium-diarylethene-framework, Chem. Eng. J. 451 (2023) 139004.

[6] C.X. Chen, Z. Wei, J.J. Jiang, Y.Z. Fan, S.P. Zheng, C.C. Cao, Y.H. Li, D. Fenske, C. Y. Su, Precise modulation of the breathing behavior and pore surface in Zr-MOFs by reversible post-synthetic variable-spacer installation to fine-tune the expansion magnitude and sorption properties, Angew. Chem. Int. Ed. 55 (2016) 9932–9936.

[7] M.J. Yin, R. Krishna, W. Wang, D. Yuan, Y.L. Fan, X.F. Feng, L. Wang, F. Luo, A $[Th_8Co_8]$ nanocage-based metal-organic framework with extremely narrow window but flexible nature enabling dual-sieving effect for both isotope and isomer separation, CCS Chem. 3 (2021) 1115–1126.

[8] Y. Zhang, X. Zhang, J. Lyu, K.I. Otake, X. Wang, L.R. Redfern, C.D. Malliakas, Z. Li, T. Islamoglu, B. Wang, O.K. Farha, A flexible metal-organic framework with 4-connected Zr_6 nodes, J. Am. Chem. Soc. 140 (2018) 11179–11183.

[9] H. Zeng, M. Xie, T. Wang, R.J. Wei, X.J. Xie, Y.F. Zhao, W.G. Lu, D. Li, Orthogonal-array dynamic molecular sieving of propylene/propane mixtures, Nature 595 (2021) 542–548.

[10] Y.G. Peng, H.L. Huang, Y.X. Zhang, C.F. Kang, S.M. Chen, L. Song, D.H. Liu, C. L. Zhong, A versatile MOF-based trap for heavy metal ion capture and dispersion, Nat. Commun. 9 (2018) 187.

[11] X.F. Wang, Y.Y. Chen, L.P. Song, Z. Fang, J. Zhang, F.N. Shi, Y.W. Lin, Y.K. Sun, Y. B. Zhang, J. Rocha, Cooperative capture of uranyl ions by a carbonyl-bearing hierarchical-porous cu-organic framework, Angew. Chem. Int. Ed. 58 (2019) 18808–18812.

[12] H. Li, S.A. Wang, Reaction: porous organic polymers for uranium capture, Chem. 7 (2021) 271–280.

[13] T. Liu, S. Tang, T. Wei, M. Chen, Z. Xie, R. Zhang, Y. Liu, N. Wang, Defect-engineered metal-organic framework with enhanced photoreduction activity toward uranium extraction from seawater, Cell Rep. Phys. Sci. 3 (5) (2022) 100892.

[14] C.R. Martin, G.A. Leith, N.B. Shustova, Beyond structural motifs: the frontier of actinide-containing metal-organic frameworks, Chem. Sci. 12 (2021) 7214–7230.

[15] H.-P. Zhang, L.-l. Gong, M.-J. Yin, X.-H. Xiong, Q.-Y. Zhang, X.-F. Feng, F. Luo, J. B. Carney, Y. Yue, Efficient organic iodide capture by a mesoporous bimetallic-organic framework, Cell Rep. Phys. Sci. 3 (4) (2022) 100830.

[16] Z. Niu, X. Cui, T. Pham, P.C. Lan, H. Xing, K. Forrest, L. Wojtas, B. Space, S.Q. Ma, A metal-organic framework based methane nano-trap for the capture of coal-mine methane, Angew. Chem. Int. Ed. 58 (2019) 10138–10141.

[17] S. Ehrling, E.M. Reynolds, V. Bon, I. Senkovska, T.E. Gorelik, J.D. Evans, M. Rauche, M. Mendt, M.S. Weiss, A. Pöppl, E. Brunner, U. Kaiser, A.L. Goodwin, S. Kaskel, Adaptive response of a metal-organic framework through reversible disorder-disorder transitions, Nat. Chem. 13 (2021) 568–574.

[18] A.P. Katsoulidis, D. Antypov, G.F. Whitehead, E.J. Carrington, D.J. Adams, N. G. Berry, G.R. Darling, M.S. Dyer, M.J. Rosseinsky, Chemical control of structure and guest uptake by a conformationally mobile porous material, Nature 565 (2019) 213–217.

[19] Y. Yang, L. Li, R.B. Lin, Y. Ye, Z. Yao, L. Yang, F.H. Xiang, S.M. Chen, Z.J. Zhang, S. C. Xiang, B.L. Chen, Ethylene/ethane separation in a stable hydrogen-bonded organic framework through a gating mechanism, Nat. Chem. 13 (2021) 933–939.

[20] S. Krause, N. Hosono, S. Kitagawa, Chemistry of soft porous crystals: structural dynamics and gas adsorption properties, Angew. Chem. Int. Ed. 59 (2020) 15325–15341.

[21] P. Vervoorts, J. Keupp, A. Schneemann, C.L. Hobday, D. Daisenberger, R. A. Fischer, R. Schmid, G. Kieslich, Configurational entropy driven high-pressure behaviour of a flexible metal-organic framework (MOF), Angew. Chem. Int. Ed. 133 (2021) 800–806.

[22] H. Zeng, M. Xie, Y.L. Huang, Y. Zhao, X.J. Xie, J.P. Bai, M.Y. Wan, R. Krishna, W. G. Lu, D. Li, Induced fit of C_2H_2 in a flexible MOF through cooperative action of open metal sites, Angew. Chem. Int. Ed. 58 (2019) 8515–8519.

[23] W. Wang, X.-H. Xiong, N.-X. Zhu, Z. Zeng, Z.-W. Wei, M. Pan, D. Fenske, J.-J. Jiang, C.-Y. Su, A rare flexible metal–organic framework based on a tailorable Mn 8 -cluster showing smart responsiveness to aromatic guests and capacity for gas separation, Angew Chem Int Ed 61 (26) (2022).

[24] S. Yuan, L. Zou, H. Li, Y.P. Chen, J. Qin, Q. Zhang, W. Lu, M.B. Hall, H.C. Zhou, Flexible zirconium metal-organic frameworks as bioinspired switchable catalysts, Angew. Chem. Int. Ed. 128 (2016) 10934–10938.

[25] E.J. Carrington, C.A. McAnally, A.J. Fletcher, S.P. Thompson, M. Warren, L. Brammer, Solvent-switchable continuous-breathing behaviour in a diamondoid metal-organic framework and its influence on CO_2 versus CH_4 selectivity, Nat. Chem. 9 (2017) 882–889.

[26] K. Roztocki, F. Formalik, A. Krawczuk, I. Senkovska, B. Kuchta, S. Kaskel, D. Matoga, Collective breathing in an eightfold interpenetrated metal-organic framework: from mechanistic understanding towards threshold sensing architectures, Angew. Chem. Int. Ed. 59 (2020) 4491–4497.

[27] H.L. Zhou, Y.B. Zhang, J.P. Zhang, X.M. Chen, Supramolecular-jack-like guest in ultramicroporous crystal for exceptional thermal expansion behaviour, Nat. Commun. 6 (2015) 6917.

[28] S.-H. Lo, L. Feng, K. Tan, Z. Huang, S. Yuan, K.-Y. Wang, B.-H. Li, W.-L. Liu, G. S. Day, S. Tao, C.-C. Yang, T.-T. Luo, C.-H. Lin, S.-L. Wang, S.J.L. Billinge, K.-L. Lu, Y.J. Chabal, X. Zou, H.-C. Zhou, Rapid desolvation-triggered domino lattice rearrangement in a metal-organic framework, Nat. Chem. 12 (1) (2020) 90–97.

[29] D. Balestri, P.P. Mazzeo, C. Carraro, N. Demitri, P. Pelagatti, A. Bacchi, Stepwise evolution of molecular nanoaggregates inside the pores of a highly flexible metal-organic framework, Angew. Chem. Int. Ed. 131 (2019) 17503–17511.

[30] Y. Wang, G. Jia, X. Cui, X. Zhao, Q. Zhang, L. Gu, L. Zheng, L.H. Li, Q. Wu, D. J. Singh, D. Matsumura, T. Tsuji, Y.-T. Cui, J. Zhao, W. Zheng, Coordination number regulation of molybdenum single-atom nanozyme peroxidase-like specificity, Chem. 7 (2) (2021) 436–449.

[31] C.X. Chen, Z.W. Wei, J.J. Jiang, S.P. Zheng, H.P. Wang, Q.F. Qiu, C.C. Cao, D. Fenske, C.Y. Su, Dynamic spacer installation for multirole metal-organic frameworks: a new direction toward multifunctional MOFs achieving ultrahigh methane storage working capacity, J. Am. Chem. Soc. 139 (2017) 6034–6037.

[32] S. Seth, S. Jhulki, Porous flexible frameworks: origins of flexibility and applications, Mater. Horiz. 8 (2021) 700–727.

[33] C. Serre, F. Millange, C. Thouvenot, M. Noguès, G. Marsolier, D. Louër, G. Férey, Very large breathing effect in the first nanoporous chromium(III)-based solids: MIL-53 or Cr^{III} $(OH)\{O_2C\text{-}C_6H_4\text{-}CO_2\}\{HO_2C\text{-}C_6H_4\text{-}CO_2H\}_xH_2O_y$, J. Am. Chem. Soc. 124 (45) (2002) 13519–13526.

[34] A. López-Olvera, J.A. Zárate, E. Martínez-Ahumada, D. Fan, M.L. Díaz-Ramírez, P. A. Sáenz-Cavazos, V. Martis, D.R. Williams, E. Sánchez-González, G. Maurin, I. A. Ibarra, SO_2 capture by two aluminum-based MOFs: rigid-like MIL-53(Al)-TDC versus breathing MIL-53(Al)-BDC, ACS Appl. Mater. Interfaces 13 (2021) 39363–39370.

[35] C. Mellot-Draznieks, C. Serre, S. Surblé, N. Audebrand, G. Férey, Very large swelling in hybrid frameworks: a combined computational and powder diffraction study, J. Am. Chem. Soc. 127 (2005) 16273–16278.

[36] P. Wang, K.I. Otake, N. Hosono, S. Kitagawa, Crystal flexibility design through local and global motility cooperation, Angew. Chem. Int. Ed. 60 (2021) 7030–7035.

[37] P. Deria, D.A. Gómez-Gualdrón, W. Bury, H.T. Schaef, T.C. Wang, P.K. Thallapally, A.A. Sarjeant, R.Q. Snurr, J.T. Hupp, O.K. Farha, Ultraporous, water stable and breathing zirconium-based metal-organic frameworks with ftw topology, J. Am. Chem. Soc. 137 (40) (2015) 13183–13190.

[38] C.X. Bezuidenhout, V.J. Smith, C. Esterhuysen, L.J. Barbour, Solvent-and pressure-induced phase changes in two 3D copper glutarate-based metal-organic frameworks via glutarate (+gauche⇄-gauche) conformational Isomerism, J. Am. Chem. Soc. 139 (2017) 5923–5929.

[39] M. Souto, J. Romero, J. Calbo, I.J. Vitórica-Yrezábal, J.L. Zafra, J. Casado, E. Ortí, A. Walsh, G. Mínguez Espallargas, Breathing-dependent redox activity in a tetrathiafulvalene-based metal-organic framework, J. Am. Chem. Soc. 140 (33) (2018) 10562–10569.

[40] R. Pallach, J. Keupp, K. Terlinden, L. Frentzel-Beyme, M. Kloß, A. Machalica, J. Kotschy, S.K. Vasa, P.A. Chater, C. Sternemann, M.T. Wharmby, R. Linser, R. S. Schmid, S. Henke, Frustrated flexibility in metal-organic frameworks, Nat. Commun. 12 (2021) 4097.

[41] T.D. Bennett, A.K. Cheetham, Amorphous metal-organic frameworks, Acc. Chem. Res. 47 (5) (2014) 1555–1562.

[42] R.N. Widmer, A.M. Bumstead, M. Jain, T.D. Bennett, J. Michler, Plasticity of metal-organic framework glasses, J. Am. Chem. Soc. 143 (49) (2021) 20717–20724.

[43] A. Karmakar, A.V. Desai, S.K. Ghosh, Ionic metal-organic frameworks (iMOFs): design principles and applications, Coord. Chem. Rev. 307 (2016) 313–341.

[44] Q. Yang, D. Liu, C. Zhong, J.-R. Li, Development of computational methodologies for metal-organic frameworks and their application in gas separations, Chem. Rev. 113 (10) (2013) 8261–8323.

[45] X.Z. Yan, F. Wang, B. Zheng, F.H. Huang, Stimuli-responsive supramolecular polymeric materials, Chem. Soc. Rev. 41 (2012) 6042–6065.

[46] Q. Gao, J. Xu, D. Cao, Z. Chang, X.H. Bu, A rigid nested metal-organic framework featuring a thermoresponsive gating effect dominated by counterions, Angew. Chem. Int. Ed. 128 (2016) 15251–15254.

[47] F. ZareKarizi, M. Joharian, A. Morsali, Pillar-layered MOFs: functionality, interpenetration, flexibility and applications, J. Mater. Chem. A. 6 (40) (2018) 19288–19329.

[48] A.L.J. Spek, Single-crystal structure validation with the program PLATON, J. Appl. Crystallogr. 36 (2003) 7–13.

[49] G. Kresse, J. Furthmüller, Efficient iterative schemes for ab initio total-energy calculations using a plane-wave basis set, Phys. Rev. B. 54 (16) (1996) 11169–11186.

[50] J.P. Perdew, K. Burke, M. Ernzerhof, Generalized gradient approximation made simple, Phys. Rev. Lett. 77 (18) (1996) 3865–3868.

[51] M.J. Hao, Z.S. Chen, H. Yang, G.I.N. Waterhouse, S.Q. Ma, X.K. Wang, Pyridinium salt-based covalent organic framework with well-defined nanochannels for efficient and selective capture of aqueous $^{99}TcO_4^-$, Sci. Bull. 67 (2022) 924–932.

[52] W. Zhou, A. Li, P.A. Gale, Q. He, A highly selective superphane for ReO_4^- recognition and extraction, Cell Rep. Phys. Sci. 3 (5) (2022) 100875.

[53] D. Ogata, J. Yuasa, Dynamic open coordination cage from nonsymmetrical imidazole-pyridine ditopic ligands for turn-on/off anion binding, Angew. Chem. Int. Ed. 58 (2019) 18424–18428.

[54] J. Li, X. Dai, L. Zhu, C. Xu, D. Zhang, M.A. Silver, P. Li, L.H. Chen, Y.Z. Li, D. W. Zuo, H. Zhang, C.L. Xiao, J. Chen, J. Diwu, O.K. Farha, T.E. Albrecht-Schmitt, Z. F. Chai, S.A. Wang, $^{99}TcO_4^-$ remediation by a cationic polymeric network, Nat. Commun. 9 (2018) 3007.

[55] S.A. Wang, E.V. Alekseev, J. Diwu, W.H. Casey, B.L. Phillips, W. Depmeier, T. E. Albrecht-Schmitt, NDTB-1: a supertetrahedral cationic framework that removes TcO_4^- from solution, Angew. Chem. Int. Ed. 122 (2010) 1075–1078.

[56] P. Bai, Z.Y. Dong, S.A. Wang, X.Y. Wang, Y. Li, Y.Z. Wang, Y.H. Ma, W.F. Yan, X. D. Zou, J.H. Yu, A layered cationic aluminum oxyhydroxide as a highly efficient and selective trap for heavy metal oxyanions, Angew. Chem. Int. Ed. 59 (2020) 19539–19544.

[57] D. Banerjee, D. Kim, M.J. Schweiger, A.A. Kruger, P.K. Thallapally, Removal of TcO_4^- ions from solution: materials and future outlook, Chem. Soc. Rev. 45 (2016) 2724–2739.

[58] J. Lin, L. Zhu, Z. Yue, C. Yang, W. Liu, T.E. Albrecht-Schmitt, J.-Q. Wang, S. Wang, $[Ln_6O_8]$ cluster-encapsulating polyplumbites as new polyoxometalate members and record inorganic anion-exchange materials for ReO_4^- sequestration, Adv. Sci. 6 (17) (2019) 1900381.

[59] S. Freye, R. Michel, D. Stalke, M. Pawliczek, H. Frauendorf, G.H. Clever, Template control over dimerization and guest selectivity of interpenetrated coordination cages, J. Am. Chem. Soc. 135 (2013) 8476–8479.

[60] J.H. Jordan, C.L. Gibb, A. Wishard, T. Pham, B.C. Gibb, Ion-hydrocarbon and/or ion-ion interactions: direct and reverse hofmeister effects in a synthetic host, J. Am. Chem. Soc. 140 (2018) 4092–4099.

[61] S. Mollick, S. Fajal, S. Saurabh, D. Mahato, S.K. Ghosh, Nanotrap grafted anion exchangeable hybrid materials for efficient removal of toxic oxoanions from water, ACS Cent. Sci. 6 (2020) 1534–1541.

[62] D.W. Zhang, T.K. Ronson, J. Mosquera, A. Martinez, J.R. Nitschke, Selective anion extraction and recovery using a $Fe_4^{II}L_4$ cage, Angew. Chem. Int. Ed. 2018 (130) (2018) 3779–3783.

[63] R. Alberto, G. Bergamaschi, H. Braband, T. Fox, V. Amendola, $^{99}TcO_4^-$: selective recognition and trapping in aqueous solution, Angew. Chem. Int. Ed. 124 (2012) 9910–9914.

[64] S.J. Pike, J.J. Hutchinson, C.A. Hunter, H-Bond acceptor parameters for anions, J. Am. Chem. Soc. 139 (2017) 6700–6706.

[65] L. Mei, F.Z. Li, J.H. Lan, C.Z. Wang, C. Xu, H. Deng, Q.Y. Wu, K.Q. Hu, L. Wang, Z. F. Chai, J. Chen, J.K. Gibson, W.Q. Shi, Anion-adaptive crystalline cationic material for $^{99}TcO_4^-$ trapping, Nat. Commun. 10 (2019) 1532.

[66] H. Xu, C.S. Cao, H.S. Hu, S.B. Wang, J.C. Liu, P. Cheng, N. Kaltsoyannis, J. Li, B. Zhao, High Uptake of ReO_4^- and CO_2 Conversion by a radiation-resistant thorium-nickle $[Th_{48}Ni_6]$ nanocage-based metal-organic framework, Angew. Chem. Int. Ed. 58 (2019) 6022–6027.

[67] Q. Sun, L. Zhu, B. Aguila, P.K. Thallapally, C. Xu, J. Chen, S. Wang, D. Rogers, S. Ma, Optimizing radionuclide sequestration in anion nanotraps with record pertechnetate sorption, Nat. Commun. 10 (2019) 1646.

[68] Y. Wang, M.S. Xie, J.H. Lan, L.Y. Yuan, J.P. Yu, J.Q. Li, J. Peng, Z.F. Chai, J. K. Gibson, M.L. Zhai, W.Q. Shi, Radiation controllable synthesis of robust covalent organic framework conjugates for efficient dynamic column extraction of $^{99}TcO_4^-$, Chem. 6 (2020) 2796–2809.

[69] J. Li, B.Y. Li, N.N. Shen, L.X. Chen, Q. Guo, L. Chen, L.W. He, X. Dai, Z.F. Chai, S. A. Wang, Task-specific tailored cationic polymeric network with high base-resistance for unprecedented $^{99}TcO_4^-$ cleanup from alkaline nuclear waste, ACS Cent. Sci. 7 (2021) 1441–1450.

[70] Z.F. Liu, K. Liu, X.J. Zheng, Y.H. Wang, X.X. Sun, P.C. Xue, C.P. Li, M. Du, Formulation of poly (ionic liquids)@COF nanotrap for efficient perrhenate sequestration from alkaline nuclear waste, Chem. Mater. 34 (2022) 5452–5460.

[71] L. Zhu, D. Sheng, C. Xu, X. Dai, M.A. Silver, J. Li, P. Li, Y. Wang, L. Chen, C. Xiao, J. Chen, R. Zhou, C. Zhang, O.K. Farha, Z.F. Chai, T.E. Albrecht-Schmitt, S. A. Wang, Identifying the recognition site for selective trapping of $^{99}TcO_4^-$ in a hydrolytically stable and radiation resistant cationic metal-organic framework, J. Am. Chem. Soc. 139 (2017) 14873–14876.

[72] Y. Li, Z. Yang, Y. Wang, Z. Bai, T. Zheng, X. Dai, S. Liu, D. Gui, W. Liu, M. Chen, L. Chen, J. Diwu, L. Zhu, R. Zhou, Z.F. Chai, T.E. Albrecht-Schmitt, S.A. Wang, A mesoporous cationic thorium-organic framework that rapidly traps anionic persistent organic pollutants, Nat. Commun. 8 (2017) 1354.

[73] D.P. Sheng, L. Zhu, X. Dai, C. Xu, P. Li, C.I. Pearce, C.L. Xiao, J. Chen, R.H. Zhou, T. Duan, O.K. Farha, Z.F. Chai, S.A. Wang, Successful decontamination of $^{99}TcO_4^-$ in groundwater at legacy nuclear sites by a cationic metal-organic framework with hydrophobic pockets, Angew. Chem. Int. Ed. 131 (2019) 5022–5026.

[74] N.N. Shen, Z. Yang, S. Liu, X. Dai, C. Xiao, K. Taylor-Pashow, D.E. Li, C. Yang, J. Li, Y.G. Zhang, M.X. Zhang, R.H. Zhou, Z.F. Chai, S.A. Wang, $^{99}TcO_4^-$ removal from legacy defense nuclear waste by an alkaline-stable 2D cationic metal-organic framework, Nat. Commun. 11 (2020) 5571.

[75] D. Sheng, L. Zhu, C. Xu, C. Xiao, Y. Wang, Y. Wang, L. Chen, J. Diwu, J. Chen, Z. F. Chai, T.E. Albrecht-Schmitt, S.A. Wang, Efficient and selective uptake of TcO_4^- by a cationic metal-organic framework material with open Ag^+ sites, Environ. Sci. Technol. 51 (2017) 3471–3479.

[76] H. Feng, X.H. Xiong, L.L. Gong, H.P. Zhang, Y. Xu, X.F. Feng, F. Luo, Rational tuning of thorium-organic frameworks by reticular chemistry for boosting radionuclide sequestration, Nano. Res. 15 (2022) 1472–1478.

[77] L. Zhu, C. Xiao, X. Dai, J. Li, D. Gui, D. Sheng, L. Chen, R. Zhou, Z.F. Chai, T. E. Albrecht-Schmitt, S.A. Wang, Exceptional perrhenate/pertechnetate uptake and subsequent immobilization by a low-dimensional cationic coordination polymer: overcoming the hofmeister bias selectivity, Environ. Sci. Technol. Lett. 4 (2017) 316–322.

Supporting information

Structural flexibility in cationic metal-organic framework for boosting ReO_4^- capture

Shufen Gu,[a] Zhiwu Yu,[b] Ning Li,[2] Qingyun Zhang,[a] Huiping Zhang,[a] Lipeng Zhang,[c] Lele Gong,[c] Rajamani Krishna[d] and Feng Luo[a]*

Correponding author: F. L. ecitluofeng@163.com

X-ray Crystallography

X-ray diffraction data were collected on a Bruker diffractometer. The data reduction included a correction for Lorentz and polarization effects, with an applied multiscan absorption correction (SADABS). The crystal structure was solved and refined using the SHELXTL program suite. Direct methods yielded all non-hydrogen atoms, which were refined with anisotropic thermal parameters. All hydrogen atom positions were calculated geometrically and were riding on their respective atoms. The SQUEEZE subroutine of the PLATON software suite was used to remove the scattering from the highly disordered guest molecules. CCDC 2201226-2201231 contains the supplementary crystallographic data of these materials, respectively. These data can be obtained free of charge from the Cambridge Crystallographic Data Centre via www.ccdc.cam.ac.uk/ data_request/cif.

Experiment for the sorption of ReO_4^-: The starting Re stock solution was made by dissolving 1.44 g NH_4ReO_4 in 1000 mL deionized water to create an 1000 mg/L (ppm) NH_4ReO_4 solution. All the adsorption experiments were conducted at 298 K.

In the sorption kinetics experiment, ReO_4^- solution with initial concentration of 65 ppm was used. The dose of adsorbent is 10 mg, while volume of ReO_4^- solution is 30 mL.

In the sorption isotherm experiment, ReO_4^- solution with initial concentration of 100-700 ppm was used. The dose of adsorbent is 10 mg, while the volume of ReO_4^- solution is 20 mL and the contact time is 5 h.

The adsorption amount, q(mg/g), was calculated by the difference of the ReO_4^- equilibrium concentration before and after adsorption (equation 1), where C_0, and C_e are the initial and equilibrium concentration of ReO_4^-, V is the volume of solution, m is the mass of used sample.

$$q = \frac{(C_0 - C_e) \times V}{m} \tag{1}$$

In the selective adsorption experiments, KNO_3, K_2CO_3, K_3PO_4, $KClO_4$ or K_2SO_4 was used to generate the mixed ion solution containing 125 ppm ReO_4^- and other ions (125 ppm) such as NO_3^-, or CO_3^{2-}, or PO_4^{3-}, or ClO_4^- , or SO_4^{2-}. The dose of adsorbent is 10 mg, while the volume of mixed ion solution is 20 mL and the contact time is 5 h.

The K_d value was determined with adsorbent of 10 mg, volume of 30 mL, ReO_4^- concentration of 1 ppm, contact time of 24 h, temprature at 298 K.

In the recycle experiments, the first adsorption was carried out with adsorbent of 10 mg, volume of 20 mL, ReO_4^- concentration of 65 ppm, contact time of 5 h, temprature at 298 K. Then the desorption was achieved by soaking ReO_4^- loaded samples in 3 M $NaNO_3$ solution (30 mL, adsorbents with NO_3^- as counterion) or 3M NaCl solution (30 mL, adsorbents with Cl^- as counterion). Then the second adsorption experiment was carried out based on the desorbed samples, except for **Co-TIB-NO₃-313** and **Co-TIB-Cl-313** adsorbents that request further redegassing under vacuum at 313 K for 24 h.

For all the adsorption test, the errors is about 3%.

The sorption data fitting by isotherm models

The Langmuir model assumes that the sorption of metal ions occurs on a homogenous surface by monolayer sorption and there no interaction between adsorbed ions, with homogeneous binding sites and equivalent sorption energies. The linear equation of the Langmuir isotherm model is expressed as followed:

$$\frac{C_e}{q_e} = \frac{1}{q_m k_L} + \frac{C_e}{q_m} \qquad (2)$$

where q_m is the maximum sorption capacity corresponding to complete monolayer coverage (mg/g) and k_L is a constant indirectly related to sorption capacity and energy of sorption (L/mg), which characterizes the affinity of the adsorbate with the adsorbent. The linearized plot was obtained when we plotted C_e/q_e against Ce and q_m and k_L could be calculated from the slope and intercept (Table S1).

The Freundlich equation is an empirical equation based on sorption on a heterogeneous surface. The isotherm assumes that adsorbent surface sites have a spectrum of different binding energies.

The linear equation can be expressed by:

$$Ln\, q_e = Ln\, k_F + \frac{1}{n} Ln\, C_e \qquad (3)$$

where k_F and n are the Freundlich constants related to the sorption capacity and the sorption intensity, respectively.

The adsorption kinetics was analyzed by simplified kinetic models such as the pseudo-first-order and pseudo-second-order, through the following two equations:

$$Ln(q_e - q_t) = Ln\, q_e - k_1 \qquad (4)$$

$$\frac{t}{q_t} = \frac{1}{k_2 \times q_e^2} + \frac{t}{q_e} \qquad (5)$$

Where q_e (mg/g) and q_t (mg/g) are the quantity of the adsorbed ReO_4^- at equilibrium and at t time, respectively, and k_1(min^{-1})/k_2[g/(mg·min)] is the pseudo-first/second-order sorption rate constant that is deduced from the slope of the plot of t/q_t versus t (Table S2).

The K_d value is calculated from the following equation,

$$K_d = \frac{V}{m} \frac{C_0 - C_e}{C_e} \qquad (6)$$

Computational Methods

The first-principle calculations were performed within the framework of density functional theory (DFT) as implemented in the plane wave set Vienna *Ab-initio* Simulation Package (VASP) code[1-2], in which the Perdew-Burke-Ernzenhof (GGA-PBE) functionalization and the project-augmented wave generalized gradient approximation pseudopotentials (PAW-GGA) were employed to calculate the exchange-correlation energy and electron-ion interaction[3-4], respectively. Additionally, spin-polarization was considered in all calculations.[5] Wave functions were expanded using a plane-wave basis set with kinetic energy cutoff of 500 eV and the geometries were fully relaxed until the residual force convergence value on each atom being less 0.02 eV Å^{-1}.[6] A gamma k-point mesh of 1×1×1 for the Brillouin zone sampling for structural optimization. During the calculations, the periodicity of MOF was maintained for simplicity and saving computational resources.

The detail of calculation of exchange energy (ΔG_a) was listed as follows. The formula of average exchange energy (ΔG_a) was defined:

$$\Delta G_a = \left[G_{\mathrm{MOF@ReO_4^-}} - G_{\mathrm{MOF@Cl^-/NO_3^-}} - 2 \times G_{\mathrm{ReO_4^-}} + 2 \times G_{\mathrm{Cl^-/NO_3^-}}\right]/2$$

Where the $G_{\mathrm{MOF@ReO_4^-}}$ and $G_{\mathrm{MOF@Cl^-/NO_3^-}}$ were the calculation total energy of the MOFs structure with $\mathrm{ReO_4^-}$, $\mathrm{Cl^-}$ or $\mathrm{NO_3^-}$ counterions. The $G_{\mathrm{ReO_4^-}}$, $G_{\mathrm{Cl^-/NO_3^-}}$ and $G_{\mathrm{NO_3^-}}$ were defaulted as the energy of freeous $\mathrm{ReO_4^-}$, $\mathrm{Cl^-}$ or $\mathrm{NO_3^-}$ ions.

[1]. G. Kresse, J. Furthmüller, *Phys. Rev. B*, 1996, 54, 11169.

[2]. G. Kresse, J. Furthmüller, *Comput. Mater. Sci.*, 1996, 6, 15.

[3]. J. P. Perdew, K. Burke, M. Ernzerhof, *Phys. Rev. Lett.*, 1996, 77, 3865.

[4]. I. V. Solvyev, P. H. Dederichs, V. I. Anisimov, *Phys. Rev. B*, 1994, 50, 16861.

[5]. L. Gong, X. Wang, T. Zheng, J. Liu, J. Wang, Y.-C. Yang, J. Zhang, X. Han, L. Zhang, Z. Xia, *J. Mater. Chem. A*, 2021, 9, 3555–3566.

[6]. L. Gong, D. Zhang, C.-Y. Lin, Y. Zhu, Y. Shen, J. Zhang X. Han, L. Zhang, Z. Xia, *Adv. Energy Mater.*, 2019, 9, 1902625.

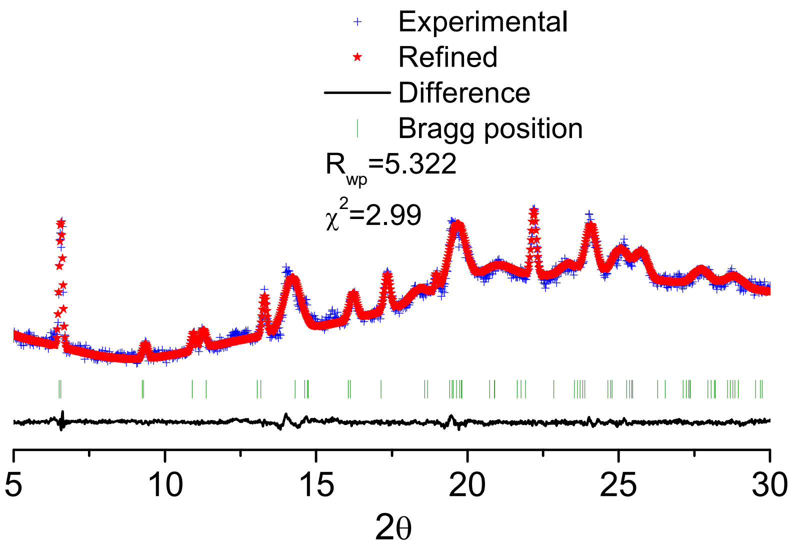

Fig. S1 A comparison between PXRD pattern of as-synthesized samples of **Co-TIB-NO$_3$** and PXRD pattern simulated from single crystal data. The refinement is using GSAS-II program.

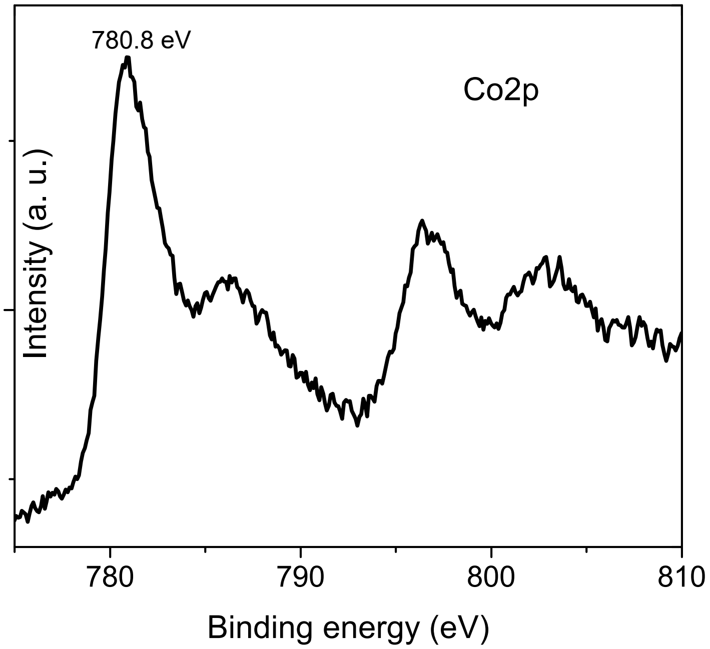

Fig. S2 The XPS of Co element in **Co-TIB-NO$_3$**. The binding energy of 780.8 eV is comparable with Co(OH)$_2$, suggesting +2 valence of Co(II) in this MOF.

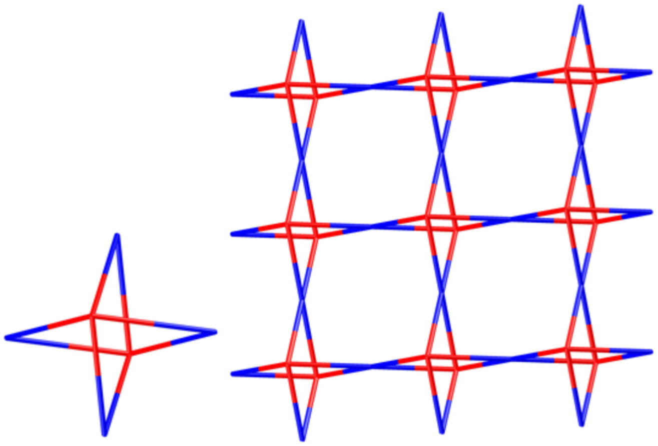

Fig. S3 View of the topology of $Co_2(TIB)_4$ cage and $Co_2(TIB)_4$ cage based double layer.

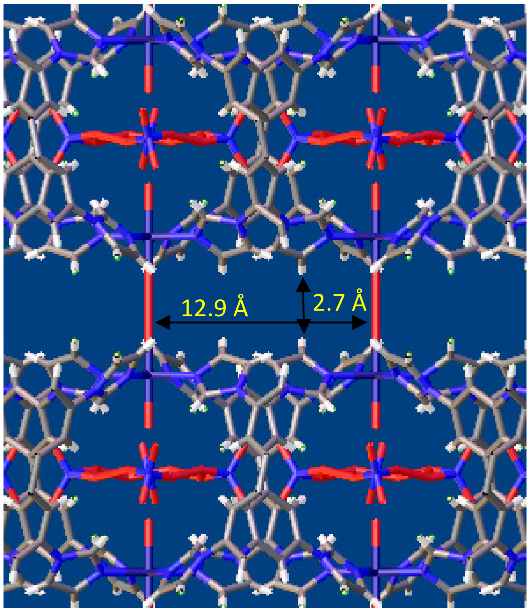

Fig. S4 View of the narrow channel in **Co-TIB-NO$_3$** along *a* or *b* direction.

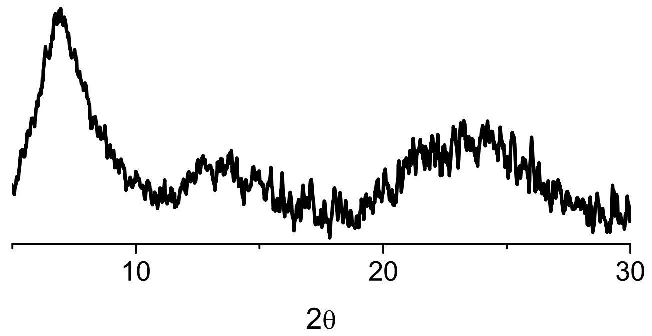

Fig. S5 The PXRD patterns of **Co-TIB-NO$_3$-313**. The broad diffuse scattering implies non-crystalline state of the resultant samples.

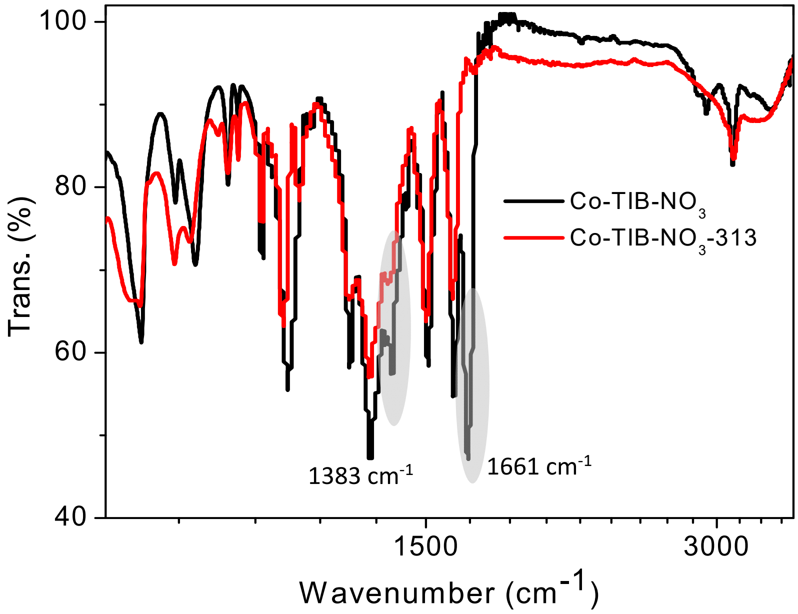

Fig. S6 A comparison of IR between **Co-TIB-NO$_3$** and **Co-TIB-NO$_3$-313**. It is found that the 1383 cm^{-1} peak belonging to NO$_3^-$ is retained, while 1661 cm^{-1} belonging to (NO$_3^-$)$_4$ tetramer disappeared, indicative of dynamic behavior of (NO$_3^-$)$_4$ tetramer.

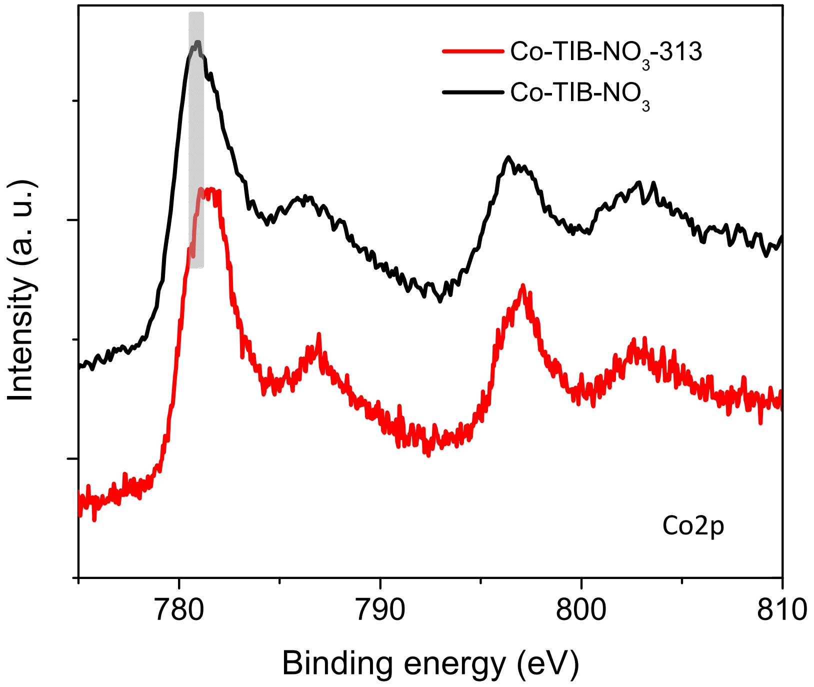

Fig. S7 A comparison of XPS of Co element between **Co-TIB-NO$_3$** and **Co-TIB-NO$_3$-313**. It is clear that Co in **Co-TIB-NO$_3$-313** shifts to higher binding energy, most likely due to interlayer compression that reinforces the additional Co-O coordination bond on the pristine pyramidal geometry.

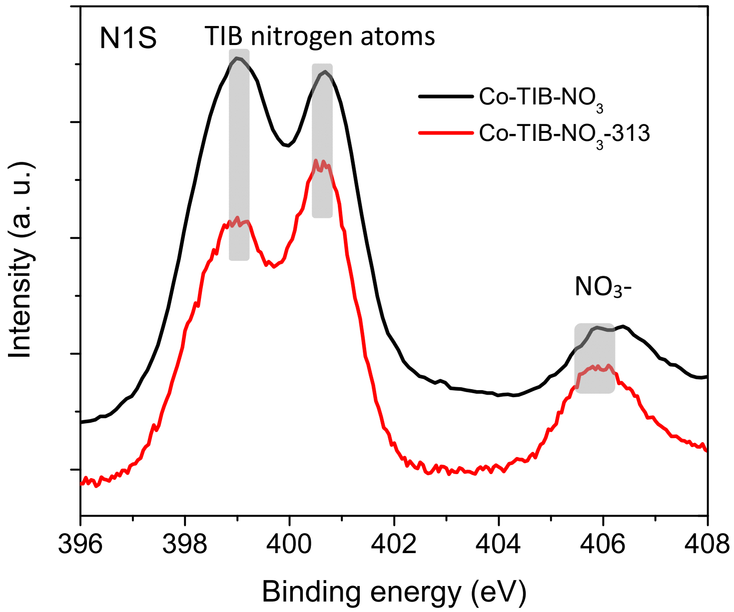

Fig. S8 A comparison of XPS of N element between **Co-TIB-NO$_3$** and **Co-TIB-NO$_3$-313**. It is clear that NO$_3^-$ in **Co-TIB-NO$_3$-313** shifts to lower binding energy, indicative of dynamic behavior of (NO$_3^-$)$_4$ tetramer.

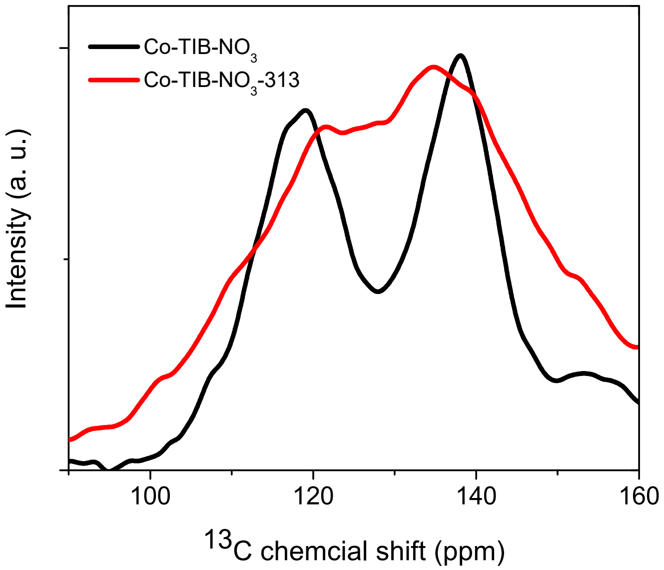

Fig. S9 A comparison of ^{13}C MAS NMR spectra between **Co-TIB-NO$_3$** and **Co-TIB-NO$_3$-313**. The broadened signals of the TIB carbon atoms suggest the disordered skeleton structure in **Co-TIB-NO$_3$-313**.

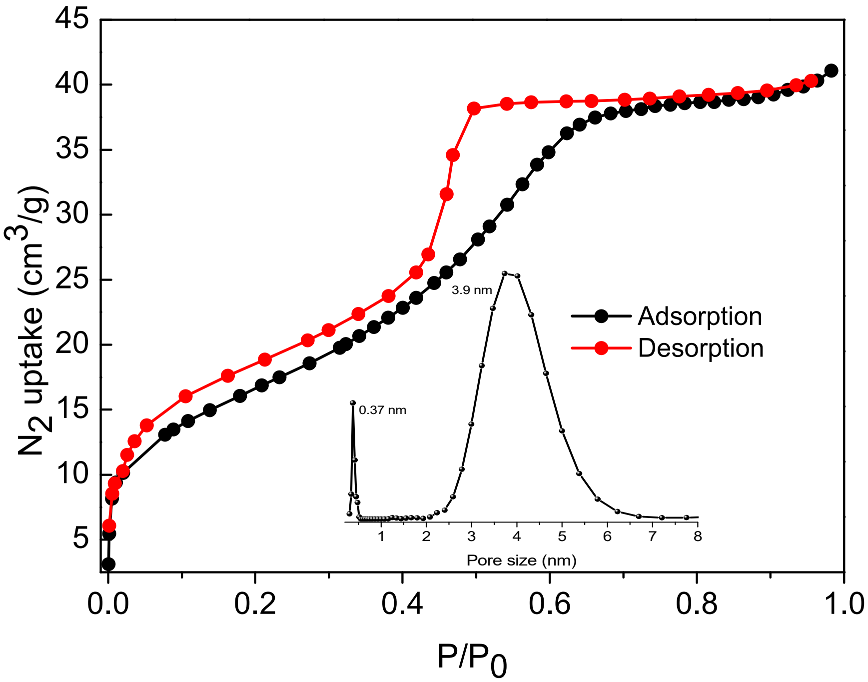

Fig. S10 The N_2 adsorption isotherm at 77 K for **Co-TIB-NO_3-313** with the inset of poree size distribution.

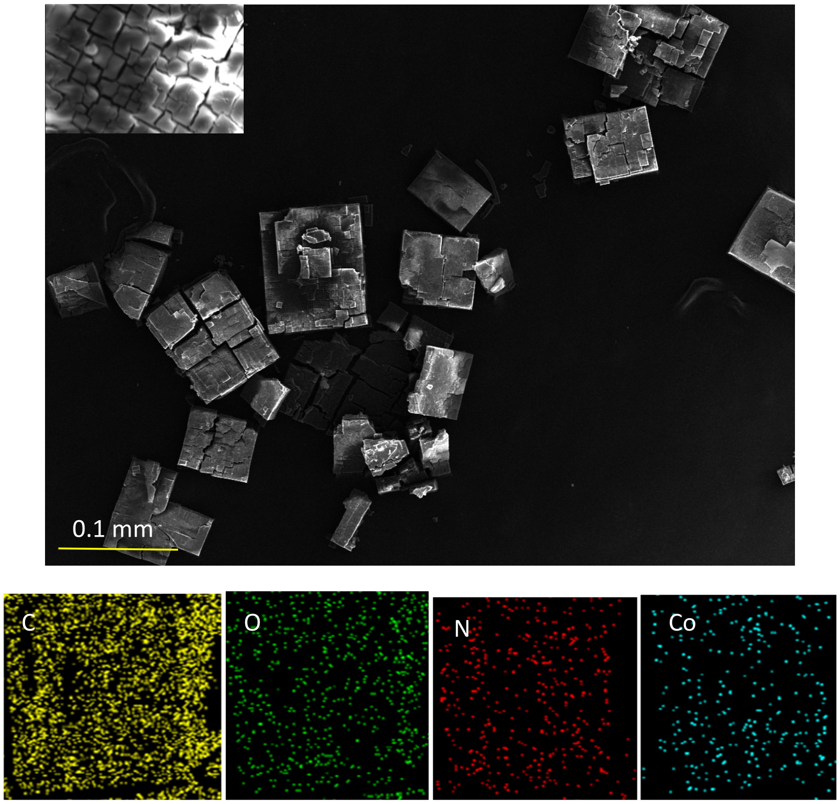

Fig. S11 The SEM images of **Co-TIB-NO$_3$-313**, where crackles were clearly observed (insert). The EDS mapping shows somewhat uneven distribution of C, O, N, and Co element, due to the disordered structure in **Co-TIB-NO$_3$-313**.

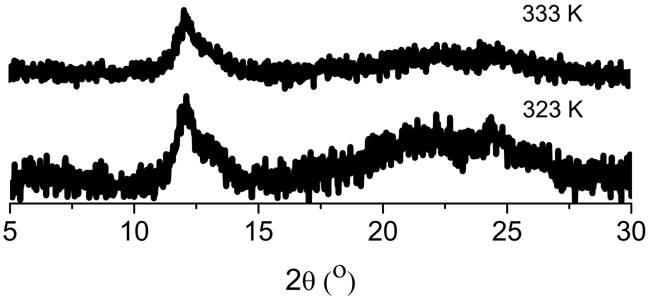

Fig. S12 The PXRD patterns of **Co-TIB-NO$_3$** samples after calcination at 323 K and 333 K for 24 h.

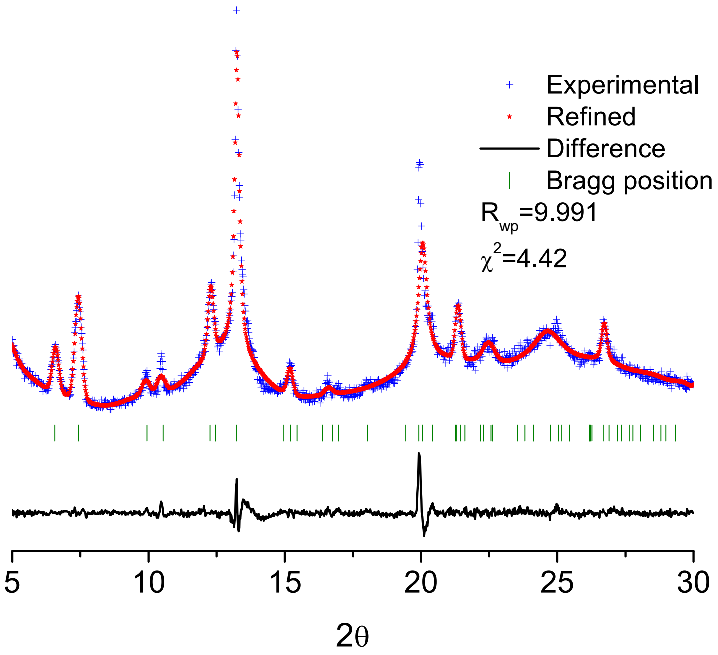

Fig. S13 A comparison between PXRD pattern of **Co-TIB-Cl-313** and PXRD pattern simulated from single crystal data. The refinement is using GSAS-II program.

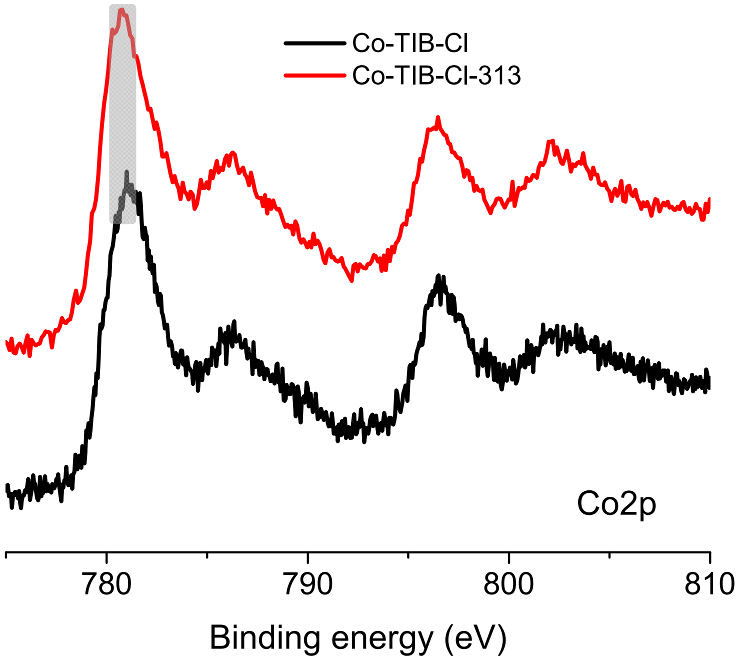

Fig. S14 A comparison of XPS of Co element between **Co-TIB-Cl** and **Co-TIB-Cl-313**, where no detectable change is observed.

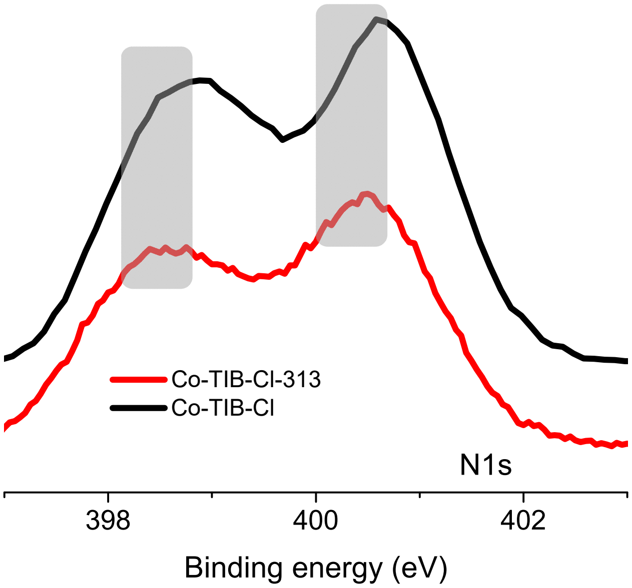

Fig. S15 A comparison of XPS of N element between **Co-TIB-Cl** and **Co-TIB-Cl-313**, where the change suggests the dynamic behavior of TIB ligand.

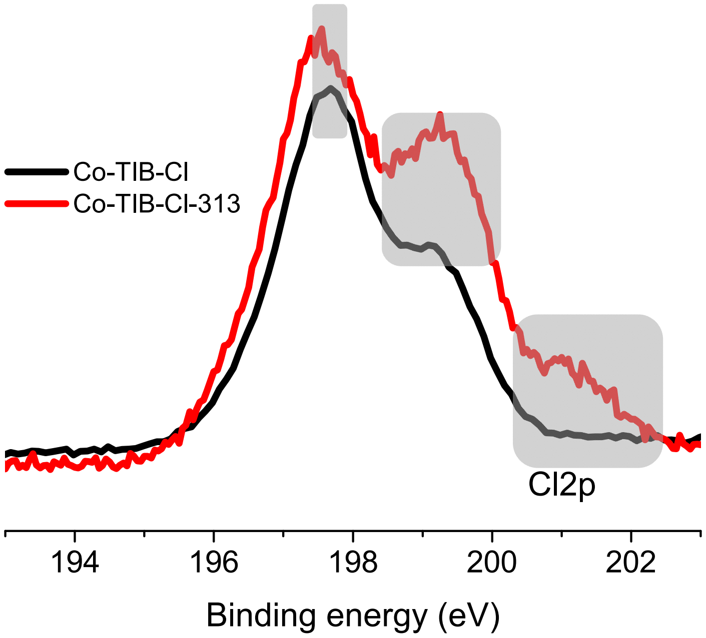

Fig. S16 A comparison of XPS of Cl element between **Co-TIB-Cl** and **Co-TIB-Cl-313**, where the change suggests the dynamic behavior of Cl^- ions.

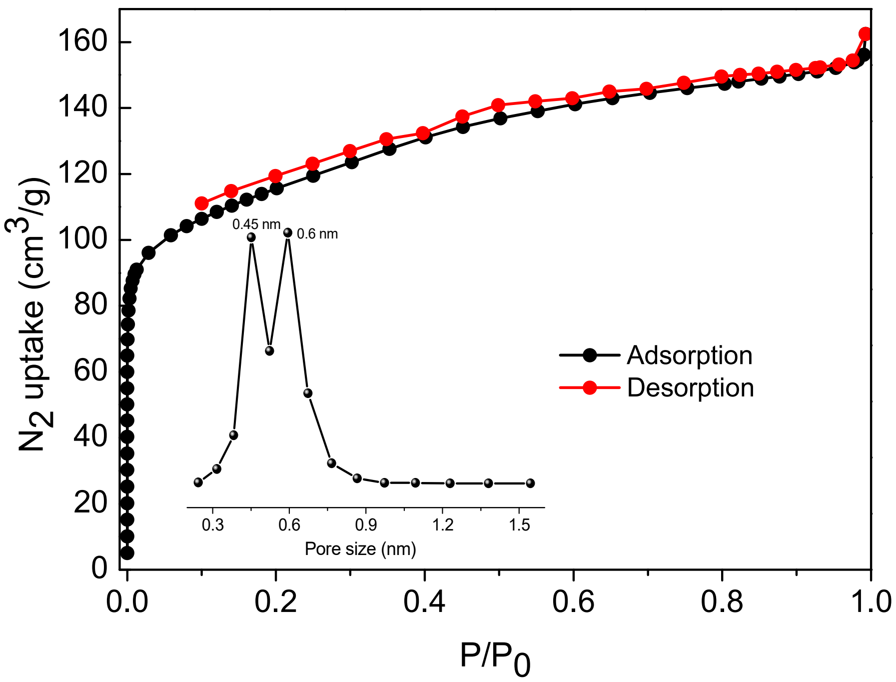

Fig. S17 The N$_2$ adsorption isotherm at 77 K for **Co-TIB-Cl-313** with the inset of poree size distribution.

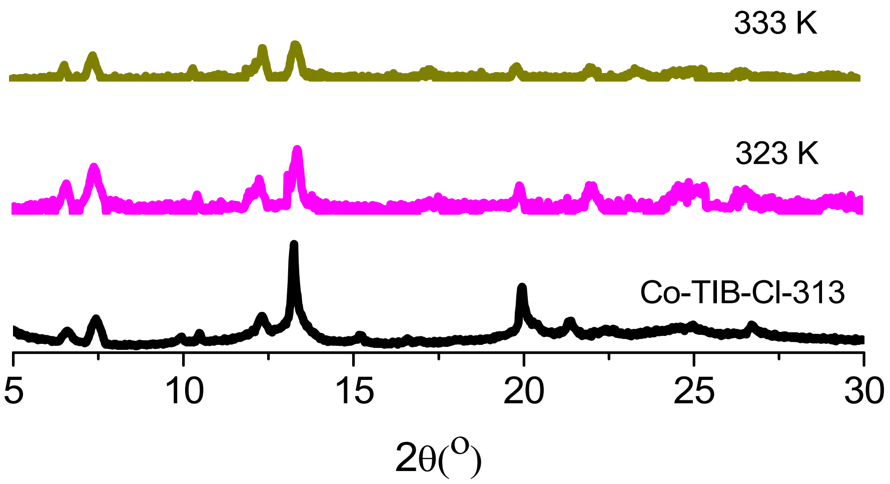

Fig. S18 The PXRD patterns of **Co-TIB-Cl** samples after calcination at 323 K and 333 K for 24 h.

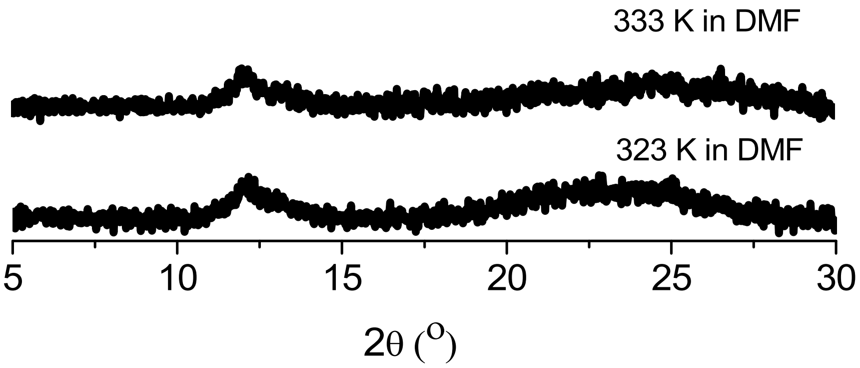

Fig. S19 The recovery of **Co-TIB-NO$_3$** samples after calcination at 323 K and 333 K for 24 h in DMF, traced by PXRD.

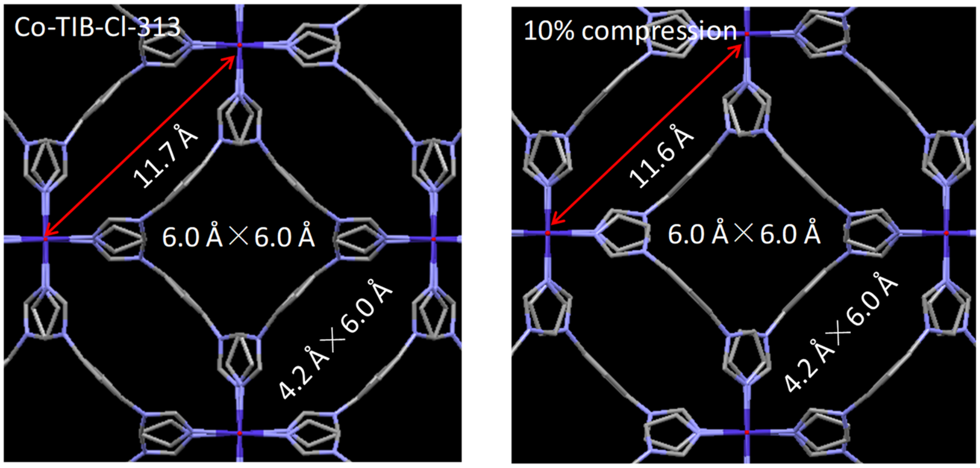

Fig. S20 A comparison of Co-TIB-Cl-313 and the calculated Co-TIB structure under 10% compression.

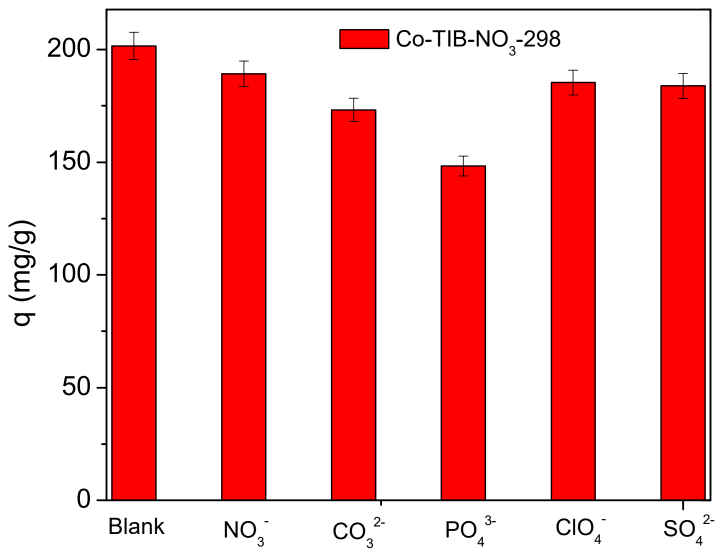

Fig. S21 Effect of competing anions on the ReO_4^- uptake by **Co-TIB-NO$_3$**.

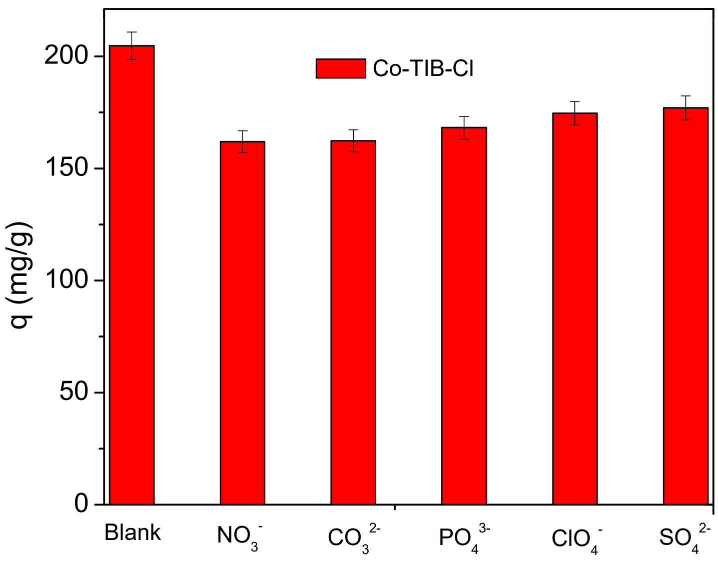

Fig. S22 Effect of competing anions on the ReO_4^- uptake by **Co-TIB-Cl**.

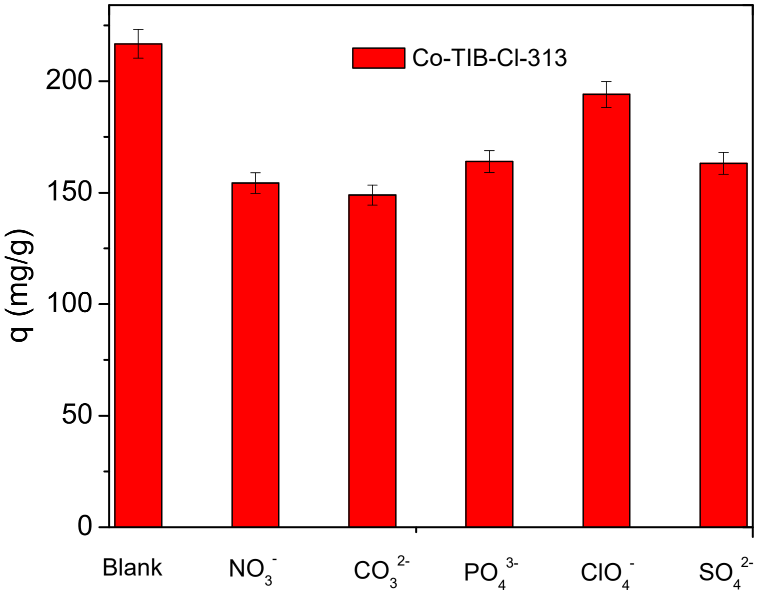

Fig. S23 Effect of competing anions on the ReO_4^- uptake by **Co-TIB-Cl-313**.

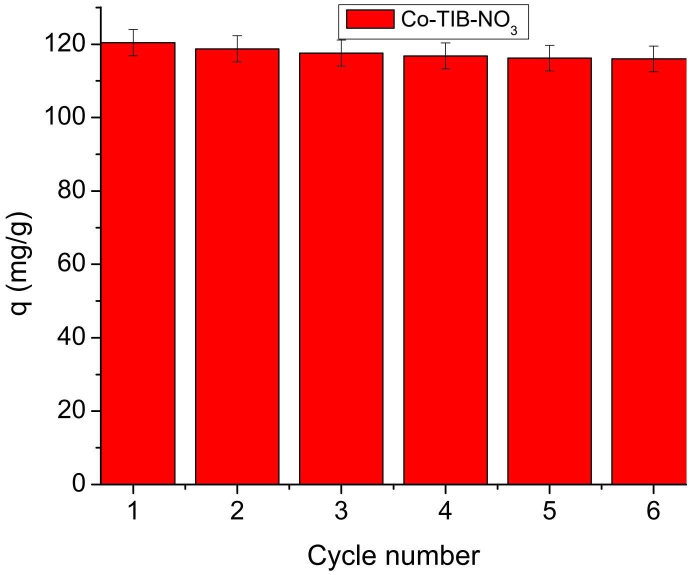

Fig. S24 Recycle use of adsorbent of **Co-TIB-NO$_3$** for ReO_4^- uptake.

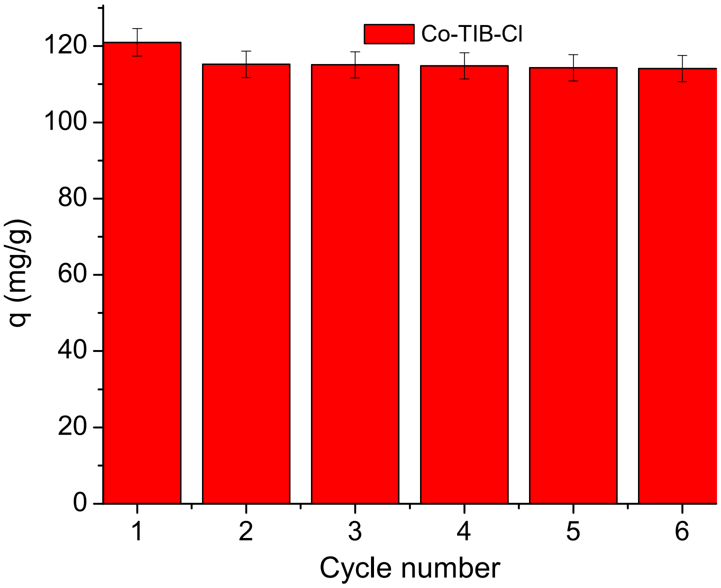

Fig. S25 Recycle use of adsorbent of **Co-TIB-Cl** for ReO_4^- uptake.

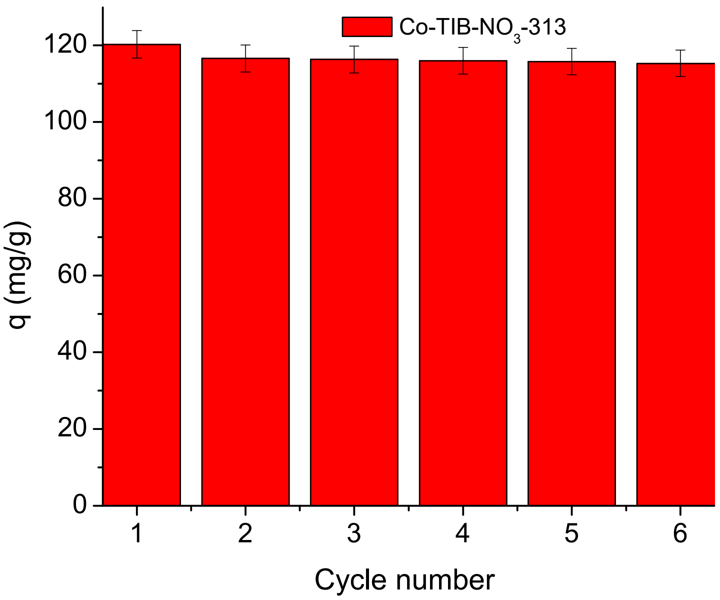

Fig. S26 Recycle use of adsorbent of **Co-TIB-NO$_3$-313** for ReO_4^- uptake.

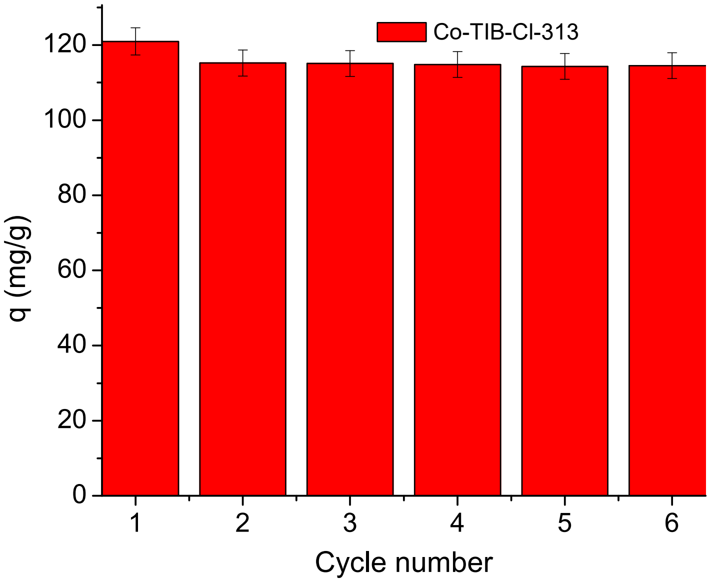

Fig. S27 Recycle use of adsorbent of **Co-TIB-Cl-313** for ReO_4^- uptake.

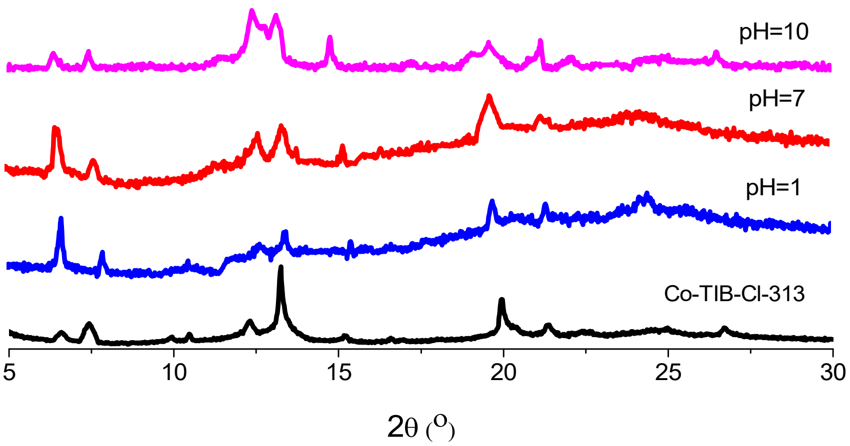

Fig. S28 The stability of **Co-TIB-NO$_3$-313** in water with various pH values. In contrast to the PXRD pattern in the crystalline CP from of Co-TIP-Cl-313, it is clear that formation of crystalline CP from was observed, when soaking **Co-TIB-NO$_3$-313** in water with pH=1, 7, and 10.

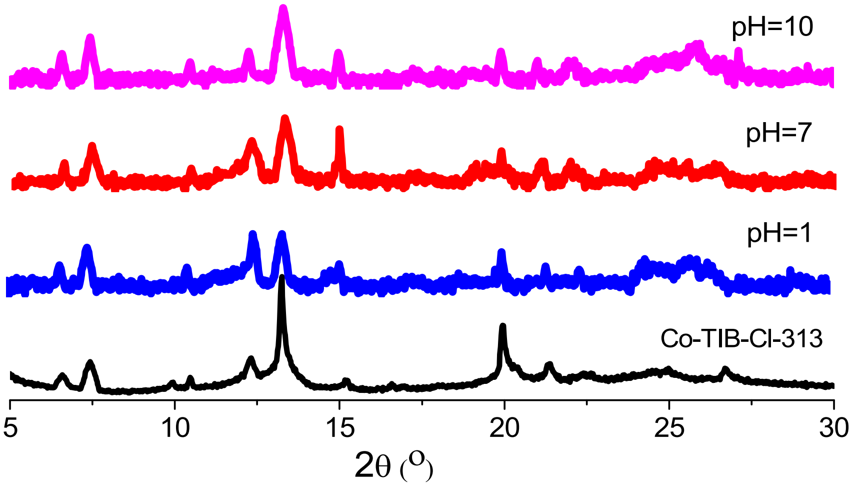

Fig. S29 The stability of **Co-TIB-Cl-313** in water with various pH values. In contrast to the PXRD pattern in the crystalline CP from of Co-TIP-Cl-313, it is clear that maintenance of crystalline CP from was observed, when soaking **Co-TIB-Cl-313** in water with pH=1, 7, and 10.

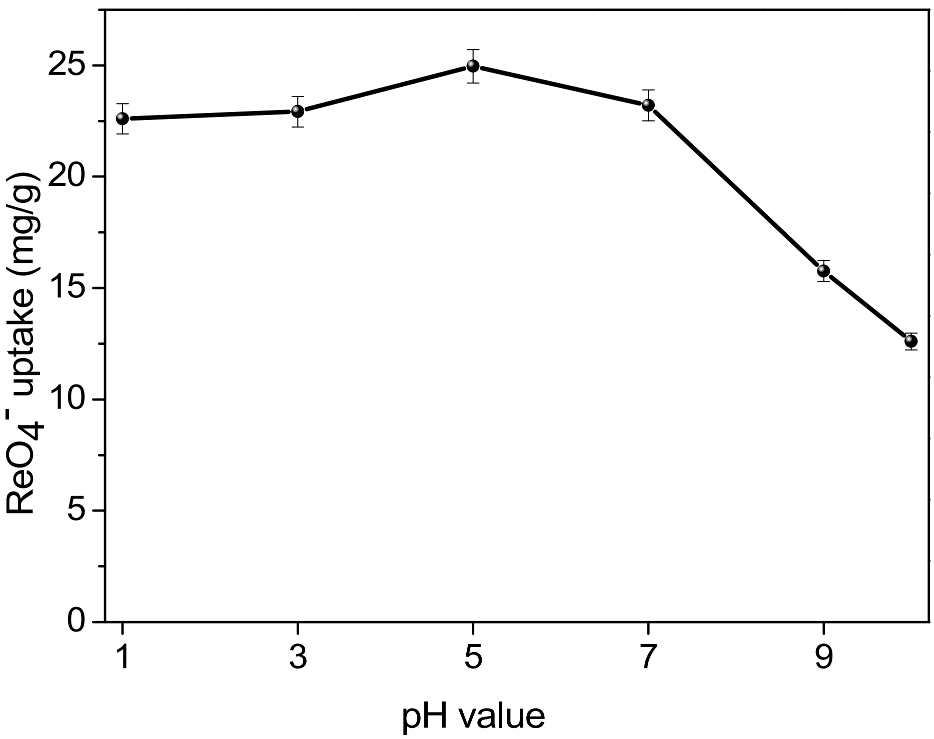

Fig. S30 View of the ReO_4^- uptake for **Co-TIB-NO_3-313** under pH=1-10 (C_0=15 ppm, m=10 mg, V=20 mL, T=298 K, Time=5 h). HNO_3 (1 M) and NaOH (1 M) was used to adjust pH value.

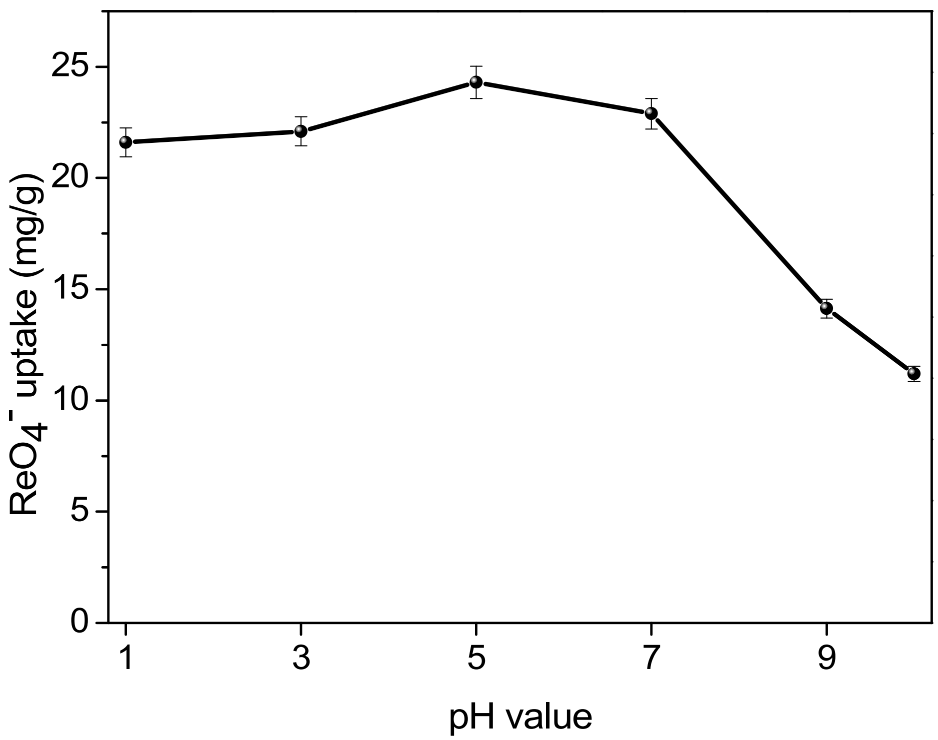

Fig. S31 View of the ReO_4^- uptake for **Co-TIB-Cl-313** under pH=1-10 (C_0=15 ppm, m=10 mg, V=20 mL, T=298 K, Time=5 h). HNO_3 (1 M) and NaOH (1 M) was used to adjust pH value.

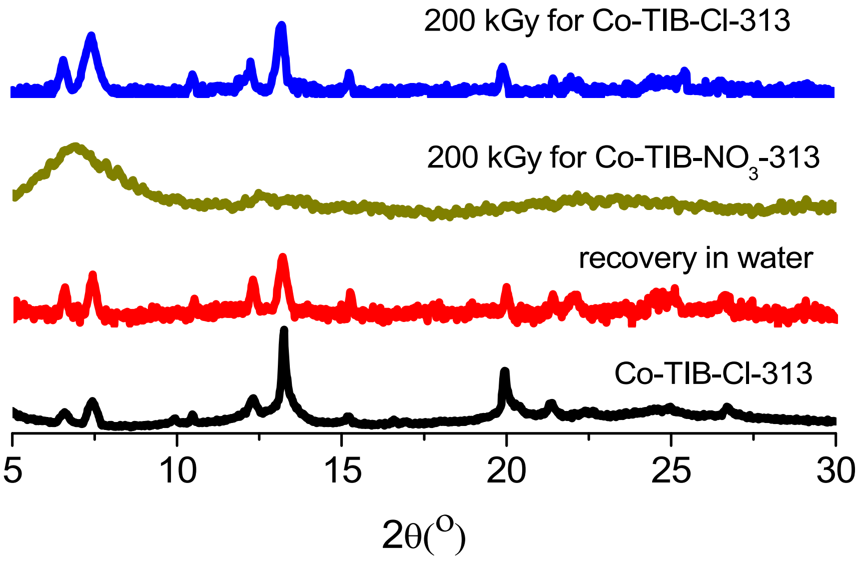

Fig. S32 PXRD patterns were used to trace the stability of these samples after β-irradiation at a dose rate of 20 kGy/h for 10 h. For samples of **Co-TIB-NO$_3$-313**, to confirm the maintenance of the integrity of the framework, the recovery to crystalline CP phase (as observed in **Co-TIB-NO$_3$-313**) was observed, when soaking corresponding samples in water.

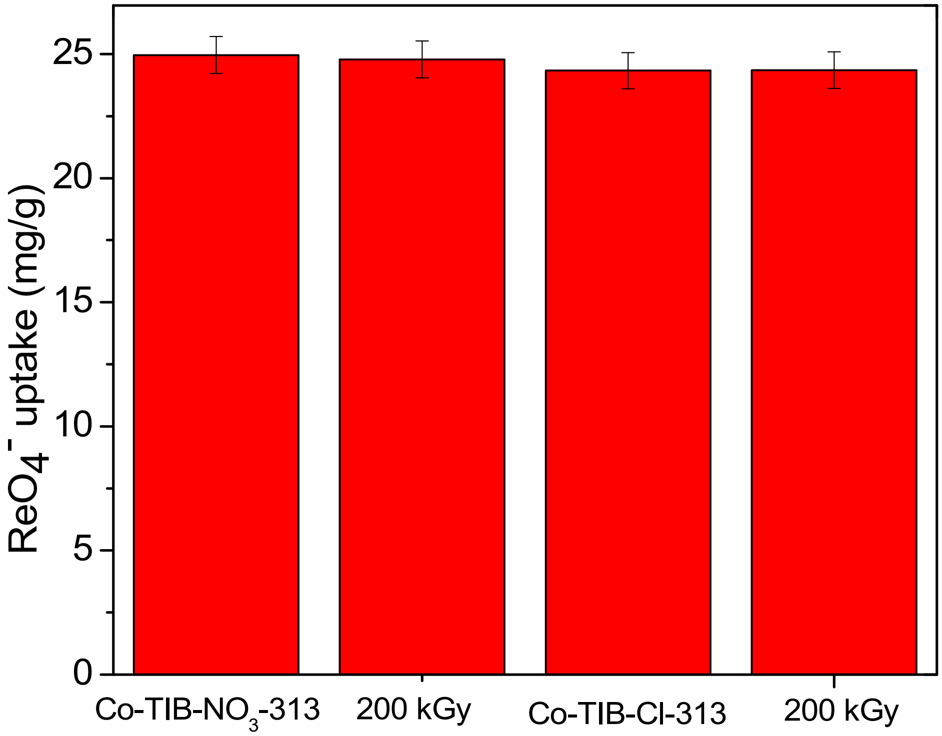

Fig. S33 A comparison of ReO_4^- uptake for the samples of **Co-TIB-NO$_3$-313** and **Co-TIB-Cl-313** before and after β-Irradiation (C_0=18 ppm, *m*=10 mg, *V*=20 mL, T=298 K, Time=5 h).

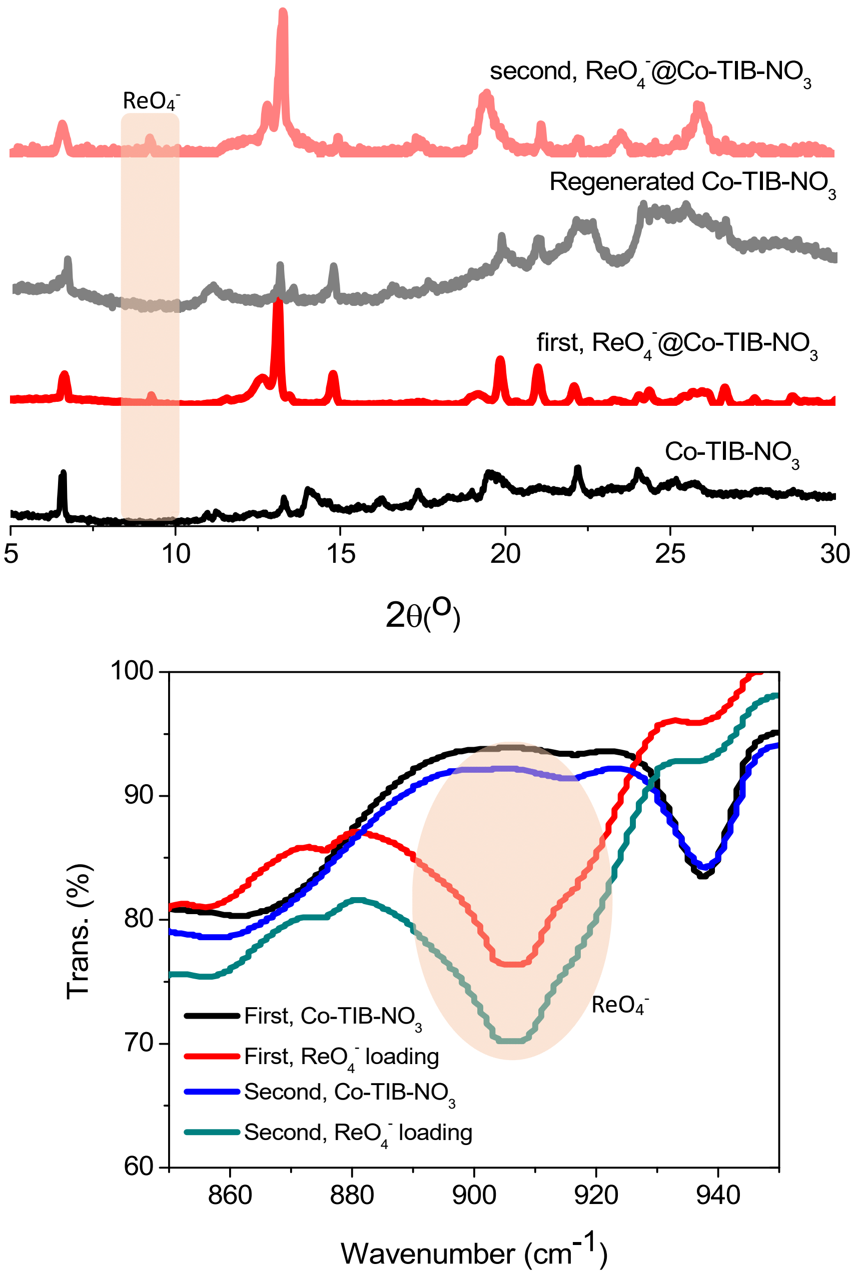

Fig. S34 A comparison of PXRD patterns and IR among the samples of **Co-TIB-NO$_3$** and its ReO_4^- loading counterpart. Two cycles was explored, where it is clear that the PXRD peak at 9.33 is due to ReO_4^- loading.

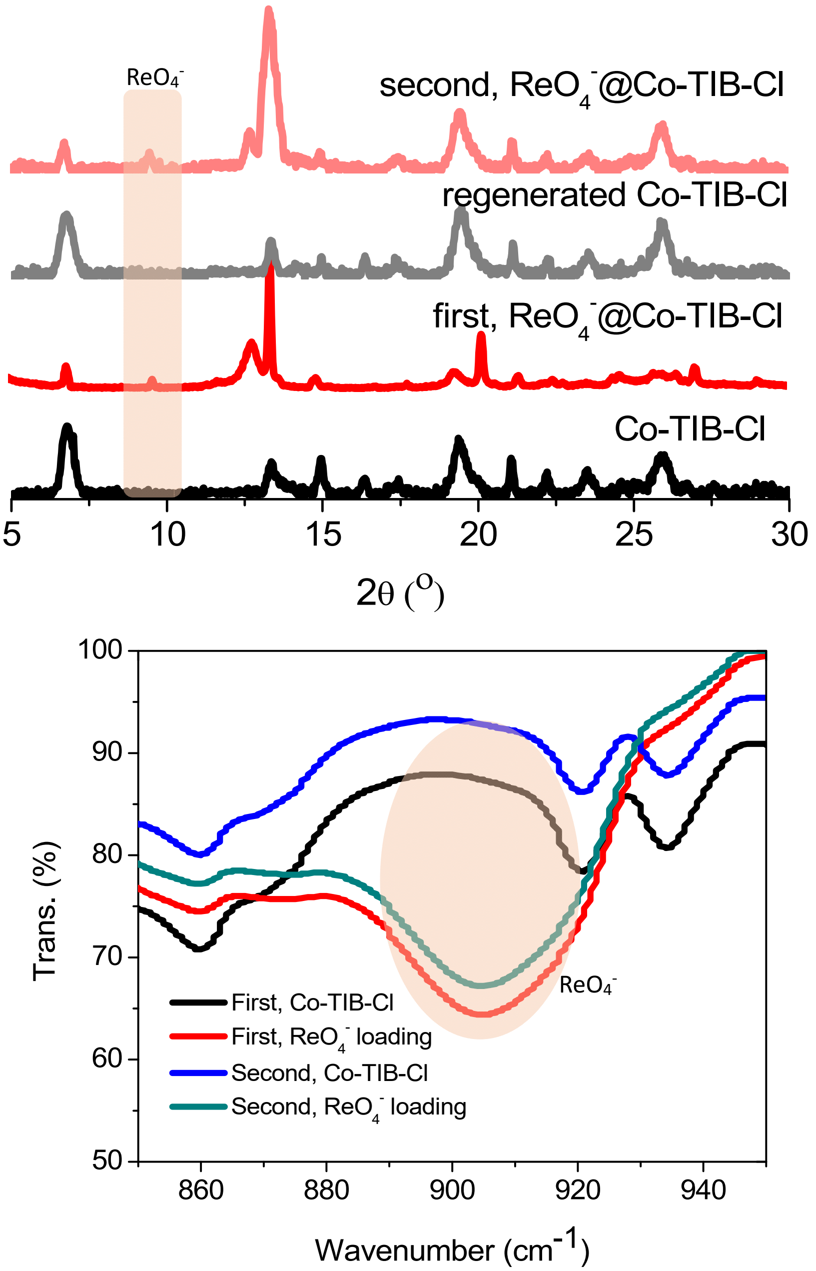

Fig. S35 A comparison of PXRD patterns and IR among the samples of **Co-TIB-Cl** and its ReO_4^- loading counterpart. Two cycles was explored, where it is clear that the PXRD peak at 9.43 is due to ReO_4^- loading.

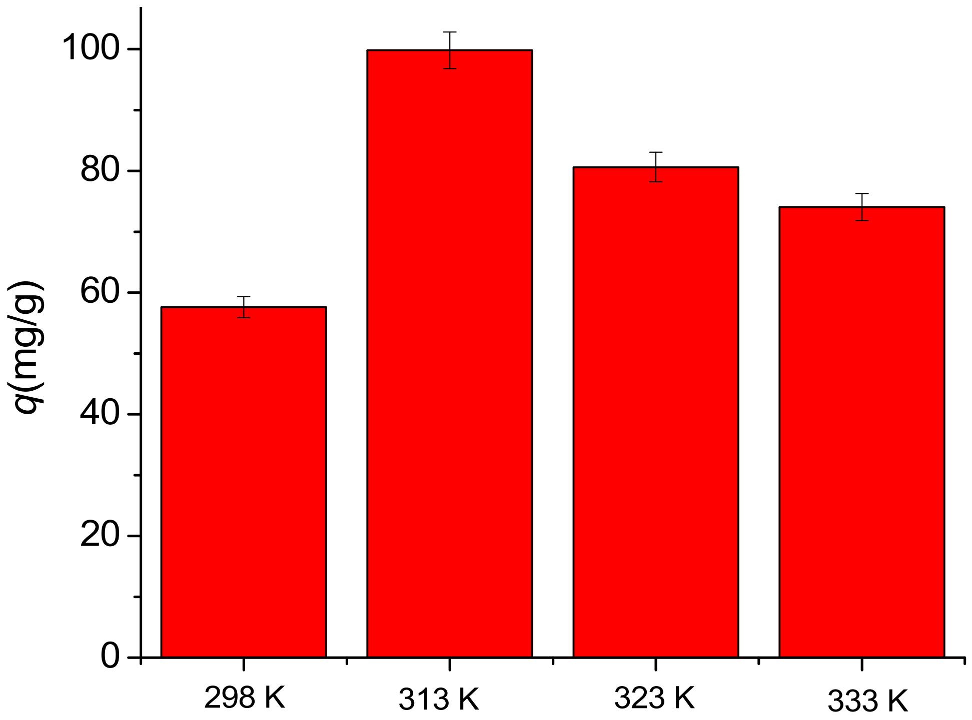

Fig. S36 A comparison of ReO_4^- uptake for NO_3^--containing samples generated at various temperature (C_0=53 ppm, *m*=10 mg, V=20 mL, T=298 K, Time=5 h).

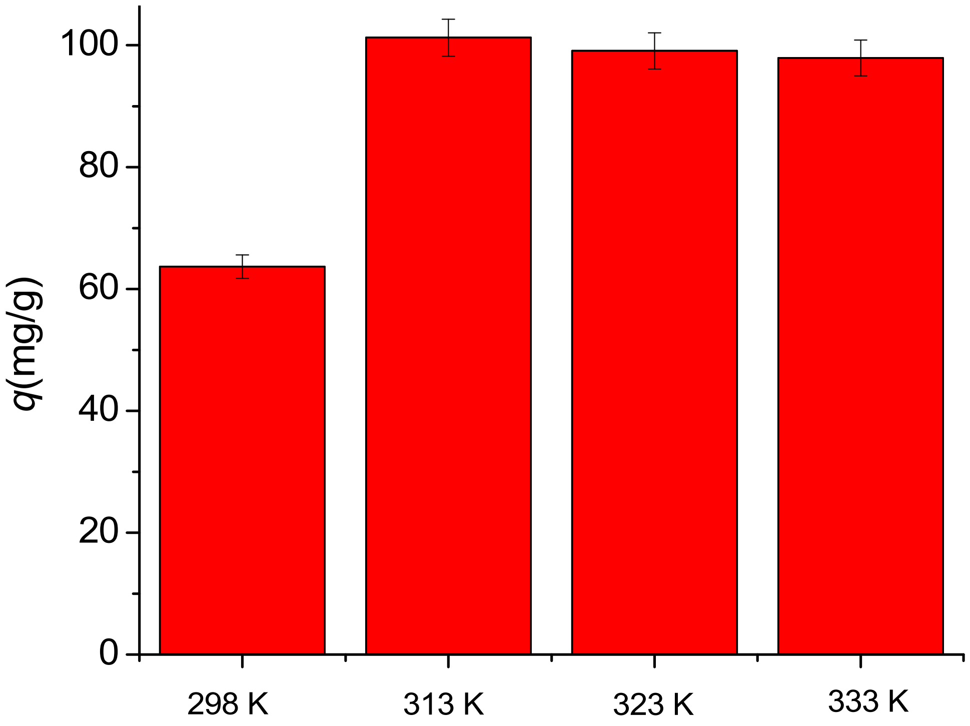

Fig. S37 A comparison of ReO_4^- uptake for Cl^--containing samples generated at various temperature (C_0=53 ppm, m=10 mg, V=20 mL, T=298 K, Time=5 h).

Table S1. A summary of the crystallographic parameters involved in this work.

Compounds	Co-TIB-NO_3	Co-TIB-NO_3-308	Co-TIB-NO_3-R	Co-TIB-Cl	Co-TIB-Cl-313	Co-TIB-Cl-R
Temperature(K)	298(2)	308(2)	240(10)	298(2)	313(2)	298(2)
Crystal system	Tetragonal	Tetragonal	Tetragonal	Tetragonal	Tetragonal	Tetragonal
Space group	I4/mcm	I4/mcm	I4/mcm	I4/mcm	I4/mcm	I4/mcm
Unit cell dimensions (Å)	18.2441(10)	18.1936(6)	18.1772(10)	18.2181(3)	16.497(2)	18.2729(10)
	18.2441(10)	18.1936(6)	18.1772(10)	18.2181(3)	16.497(2)	18.2729(10)
	26.915(4)	26.897(2)	26.738(2)	26.3120(9)	26.594(6)	26.293(4)
Volume (Å^3)	8958.6(15)	8903.3(8)	8834.5(12)	8732.9(4)	7238(2)	8779.3(14)
R indices (all data)	R1=0.1225	R1=0.1773	R1=0.0705	R1=0.1189	R1=0.1882	R1=0.1218
	wR_2= 0.2233	wR_2=0.3032	wR_2= 0.1960	wR_2=0.3433	wR_2=0.3404	wR_2=0.2638
CCDC number	2201231	2201226	2201228	2201230	2201227	2201229

For Cl-replaced samples (generated 323 K, and 333 K), the recovery to crystalline OP form was confirmed by the determination of unit cell, giving a=b=18.1648(9), c=26.274 (3) for 323 K and a=b=18.3317 (10), c=26.165 (4) for 333 K.

Table S2. Kinetic parameters of pseudo-first-order and pseudo-second-order models.

Adsorbent	$q_{e,\text{exp}}$ (mg·g^{-1})	pseudo-first-order			pseudo-second-order		
		$q_{e,\text{cal}}$ (mg·g^{-1})	k_1 (min^{-1})	R^2	$q_{e,\text{cal}}$ (mg·g^{-1})	k_2 (g·mg^{-1}·min^{-1})	R^2
Co-TIB-NO$_3$	146.41	122.067	0.0664	0.8550	156.006	0.00038	0.9967
Co-TIB-Cl	152.54	79.815	0.0489	0.9114	156.740	0.00082	0.9999
Co-TIB-NO$_3$-313	186.36	138.951	0.0737	0.9602	196.078	0.00044	0.9989
Co-TIB-Cl-313	188.51	113.750	0.0422	0.9376	194.932	0.00048	0.9994

Table S3. Isotherm parameters of Langmuir and Freundlich models.

Adsorbent	Langmuir model				Freundlich model		
	$q_{e,\text{exp}}$ (mg·g^{-1})	K_L (L·mg^{-1})	q_m (mg·g^{-1})	R^2	K_F (mg$^{1-1/n}$·g^{-1}·L$^{-1/n}$)	$1/n$	R^2
Co-TIB-NO$_3$	284.18	0.0113	348.432	0.9858	24.403	0.4199	0.8883

Co-TIB-Cl	391.71	0.0250	427.350	0.9931	98.727	0.2319	0.9836
Co-TIB-NO_3-313	539.55	0.0206	613.497	0.9958	71.243	0.3571	0.9523
Co-TIB-Cl-313	460.77	0.0182	507.614	0.9934	78.038	0.2968	0.9758

Table S4. A comparison table of ReO_4^- capture with some well-studied examples in the literature.

	Compounds	Uptake capacity (mg/g)	Reference
MOFs	UIO-66-NH_3^+Cl	159	Inorg. Chem. 2016, 55, 8241-8243
	NU-1000	210	Chem. Mater. 2018, 30, 1277-1284
	SCU-101	217	J. Am. Chem. Soc. 2017, 139, 14873-14876
	SCU-103	318	Nat. Commun. 2020, 11, 5571
	Co-TIB-NO_3	281	Our work
	Co-TIB-Cl	392.9	Our work
	Co-TIB-Cl-313	459.6	Our work
	Co-TIB-NO_3-313	540	Our work
	SCU-100	553	Environ. Sci. Technol. 2017, 51, 3471-3479
	Th-MOF-68	560	Nano. Res. 2022, 15, 1472-1478
	SLUG-21	602	J. Am. Chem. Soc. 2010, 132, 7202-7209
	iMOF-2C	691	ACS Appl. Mater. Inter. 2020, 12, 41810-41818
	CAU-1	692	J. Hazard. Mater. 2021, 407, 5, 124729
	SBN	786	Environ. Sci. Technol. Lett. 2017, 4, 316-322
	Th-MOF	807	Angew. Chem. Int. Ed. 2019, 131, 6083-6088
	MOR-2	1025	J. Mater. Chem. A, 2018, 6, 20813-20821
Inorganic compounds	MgAl-LDHs	112	Water Res. 2009, 43, 3067-3075
	YPbOClO_4-1	434	Adv. Sci. 2019, 6, 1900381
Polymer	PAF-1-F	420	Chem. Eur. J. 2016, 22, 17581-17584
	SCU-CPN-1	999	Nat. Commun. 2018, 9, 3007
	PQA-pN$(Me)_2$Py-Cl	1127	Nat Commun. 2019, 10, 1646
	SCU-CPN-2	1467	Sci. China Chem. 2021, 64, 1251-1260
COFs	PS-COF-1	1262	Sci. Bull. 2022, 67, 924-932
	NKCOF-41-Cl^-	1078	Angew. Chem. Int. Ed. 2022, 61, e202213247